

# ALMANAC: WEAK LENSING POWER SPECTRA AND MAP INFERENCE ON THE MASKED SPHERE

ARTHUR LOUREIRO

Institute for Astronomy, University of Edinburgh, Royal Observatory, Blackford Hill, Edinburgh EH9 3HJ, UK  
 Department of Physics and Astronomy, University College London, Gower Street, London WC1E 6BT, UK  
 Astrophysics Group and Imperial Centre for Inference and Cosmology (ICIC), Blackett Laboratory, Imperial College London, Prince Consort Road, London SW7 2AZ, UK

LORNE WHITEWAY

Department of Physics and Astronomy, University College London, Gower Street, London WC1E 6BT, UK

ELENA SELLENTIN

Mathematical Institute, Leiden University, Snellius Gebouw, Niels Bohrweg 1, NL-2333 CA Leiden, The Netherlands  
 Leiden Observatory, Leiden University, Oort Gebouw, Niels Bohrweg 2, NL-2333 CA Leiden, The Netherlands

JAVIER SILVA LAFAURIE

Mathematical Institute, Leiden University, Snellius Gebouw, Niels Bohrweg 1, NL-2333 CA Leiden, The Netherlands  
 Leiden Observatory, Leiden University, Oort Gebouw, Niels Bohrweg 2, NL-2333 CA Leiden, The Netherlands

ANDREW H. JAFFE

Astrophysics Group and Imperial Centre for Inference and Cosmology (ICIC), Blackett Laboratory, Imperial College London, Prince Consort Road, London SW7 2AZ, UK

ALAN F. HEAVENS

Astrophysics Group and Imperial Centre for Inference and Cosmology (ICIC), Blackett Laboratory, Imperial College London, Prince Consort Road, London SW7 2AZ, UK  
*Version October 25, 2022*

## ABSTRACT

We present a field-based signal extraction of weak lensing from noisy observations on the curved and masked sky. We test the analysis on a simulated Euclid-like survey, using a Euclid-like mask and noise level. To make optimal use of the information available in such a galaxy survey, we present a Bayesian method for inferring the angular power spectra of the weak lensing fields, together with an inference of the noise-cleaned tomographic weak lensing shear and convergence (projected mass) maps. The latter can be used for field-level inference with the aim of extracting cosmological parameter information including non-gaussianity of cosmic fields. We jointly infer all-sky  $E$ -mode and  $B$ -mode tomographic auto- and cross-power spectra from the masked sky, and potentially parity-violating  $EB$ -mode power spectra, up to a maximum multipole of  $\ell_{\max} = 2048$ . We use Hamiltonian Monte Carlo sampling, inferring simultaneously the power spectra and denoised maps with a total of  $\sim 16.8$  million free parameters. The main output and natural outcome is the set of samples of the posterior, which does not suffer from leakage of power from  $E$  to  $B$  unless reduced to point estimates. However, such point estimates of the power spectra, the mean and most likely maps, and their variances and covariances, can be computed if desired.

## 1. INTRODUCTION

Cosmic shear analysis has developed over the past few decades into a powerful cosmological probe for studying the large-scale structure of the Universe (Bartelmann & Schneider 2001; Munshi et al. 2008; Kilbinger 2015). Photons from distant galaxies travel towards us along geodesic paths that are distorted by the gravitational potential of dark and baryonic matter along the way. The result is a coherent distortion in the observed shapes of

background galaxies: a weak gravitational lensing effect that shears and magnifies objects (Bartelmann & Schneider 2001). The shape distortions are sensitive to the total matter content of the Universe and its clustering (Hall 2021), and so this effect makes cosmic shear an effective probe for studying the growth of structure and the geometric evolution of the Universe (Heavens 2009). Measuring how the gravitational potential along the line-of-sight affects the ellipticities of galaxies in photometric galaxy surveys also allows us to map the invisible distribution of dark matter around galaxies (Kaiser & Squires 1993; Marshall et al. 2002; Lanusse et al. 2016; Jeffrey et al. 2021; Wallis et al. 2022) and to understand the structure of the cosmic web (Rossi 2012; Joachimi et al. 2015; Codis et al. 2018).

arthur.loureiro@ed.ac.uk  
 lorne.whiteway@star.ucl.ac.uk  
 sellentin@strw.leidenuniv.nl  
 silvalafaurie@strw.leidenuniv.nl  
 a.jaffe@imperial.ac.uk  
 a.heavens@imperial.ac.uk

Recent years have seen an impressive increase in both the quality and quantity of weak lensing data and analysis techniques. Current photometric surveys such as the Kilo Degree Survey (KiDS; Heymans et al. 2021; Asgari et al. 2021; Loureiro et al. 2022), the Dark Energy Survey (DES; DES Collaboration et al. 2022; Amon et al. 2022; Secco et al. 2022), and the Subaru Hyper Supreme-Cam survey (HSC; Mandelbaum et al. 2018; Hikage et al. 2019) have, together, revolutionised cosmology by using cosmic shear to challenge its standard model. Contemporary weak lensing experiments infer a growth of structure parameter ( $S_8$ ) that is in tension with the value inferred from the cosmic microwave background (CMB) (Heymans et al. 2013; MacCrann et al. 2015; Lemos et al. 2021; Amon & Efstathiou 2022).

New data from forthcoming cosmic shear surveys such as Euclid (Laureijs et al. 2011) and LSST (LSST Science Collaboration et al. 2009), combined with improved data analysis techniques, could shed light on this tension and help us better understand the geometry and growth of structure in the Universe. These future weak lensing experiments will measure the shapes of billions of galaxies across large portions of the sky with unprecedented accuracy and precision. The question ‘how to extract optimally the cosmic shear information from these data?’ is hotly debated in the field (Kilbinger et al. 2014; Jarvis 2015; Alonso et al. 2019; Nicola et al. 2021; Asgari et al. 2021; Porqueres et al. 2021, 2022).

The vastly increased precision expected from Euclid and LSST raises the question of whether the traditional approach of summary statistics such as correlation functions and pseudo-power spectrum estimates are accurate enough for robust inference. There is some evidence that shear correlation functions fail (Hartlap et al. 2009; Sellentin & Heavens 2018; Sellentin et al. 2018), while pseudo- $C_\ell$  estimates are close to gaussian (Upham et al. 2022). Avoiding having to assume the gaussianity of such summaries is a major benefit of field-level inference approaches, whose goal is to sample correctly from the likelihood of the (close to) raw field-level data.

There are two general approaches to field-level inference of cosmic shear: one firmly based in a cosmological model with a physical gravity model, the other (the approach taken in this paper) more agnostic, inferring the underlying shear maps and their two-point statistics in a cosmology-independent way with minimal assumptions.

In an example of the former, model-based approach, Porqueres et al. (2022) showed that FLI can strongly lift the standard ‘banana’ cosmic shear parameter degeneracy (the degeneracy between the amplitude of matter density fluctuations  $\sigma_8$  and the total matter density  $\Omega_m$ ). By extending the BORG framework (Jasche & Wandelt 2013; Jasche & Lavaux 2019), which includes a full gravity model, sampling of the initial gaussian density field is performed and forward modelled to the tomographic shear fields, where the likelihood is applied. This is a very powerful framework, but it ties the inference to a particular cosmological model.

The approach of this work – as embodied in our algorithm, called ALMANAC – is complementary, inferring the shear maps and the power spectra of the (denoised, unmasked) fields in a cosmology-independent way. The samples of maps and power spectra produced by ALMANAC are not tied to a particular model (beyond a few

basic symmetry assumptions), and can subsequently be used for parameter inference (although the goal of this paper is simply to draw map and power spectra samples). The main challenge is efficient scaling with the highest multipole probed, so we concentrate on a relatively simple 2-bin tomographic example. More details of ALMANAC are presented in a companion paper (Sellentin, Loureiro et al., *in prep*).

The paper is structured as follows: weak lensing theory in section 2 is followed by the hierarchical data model in section 3, and the Cholesky reparameterisation in section 4. Simulations are described in section 5, and results and convergence tests presented in section 6. We give our conclusions in section 7.

## 2. WEAK LENSING THEORY

Galaxies are biased tracers of the dark matter density field. By contrast, weak distortions in the observed shapes of background galaxies (caused by the deflection of light by foreground structures) are an excellent tracer of the projected matter field. This section outlines the formalism behind using this weak lensing as a cosmological probe. Further details can be found in reviews by Bartelmann & Schneider (2001) and Kilbinger (2015).

The usual approximation of the lens equation maps the unperturbed two-dimensional source angular position  $\theta_s$  to the observed position  $\theta_{\text{obs}}$  via a mapping  $A_{ij}$ :  $\theta_{s,i} \approx A_{ij}\theta_{\text{obs},j}$ . This mapping can be expressed in terms of the effective lensing potential  $\tilde{\Psi}$  as

$$A_{ij} = \delta_{ij} - \partial_i \partial_j \tilde{\Psi}, \quad (1)$$

where  $\tilde{\Psi}$  is a weighted projection along the line-of-sight of the three-dimensional Newtonian potential  $\Psi$  (Kaiser 1992):

$$\tilde{\Psi}(\chi_s, \hat{n}) = 2 \int_0^{\chi_s} d\chi \frac{f_K(\chi_s - \chi)}{f_K(\chi)f_K(\chi_s)} \Psi(\chi, \hat{n}). \quad (2)$$

Here  $\chi_s$  is the comoving distance to the lensing source, and  $f_K$  is related to the curvature  $K$  of the universe (for a flat universe  $f_{K=0}(\chi) = \chi$ , where  $\chi$  is a comoving distance variable). We also define the tomographic-bin averaged quantity

$$\tilde{\Psi}(\hat{n}) = \int d\chi \bar{n}(\chi) \tilde{\Psi}(\chi, \hat{n}) \quad (3)$$

where  $\bar{n}(\chi)$  is the normalised density of sources (averaged over the sky);  $\tilde{\Psi}$  is a scalar (i.e. spin-0) field on the sky.

The mapping in Eq. (1) can also be written in terms of the spin-0 lensing convergence field  $\kappa$  and the complex spin-2 shear field  $\gamma = \gamma_1 + i\gamma_2$ :

$$\mathbf{A} = \begin{pmatrix} 1 - \kappa - \gamma_1 & -\gamma_2 \\ -\gamma_2 & 1 - \kappa + \gamma_1 \end{pmatrix}. \quad (4)$$

The potentially observable quantities  $\kappa$  and  $\gamma$  are related to the lensing potential  $\tilde{\Psi}$  by

$$\kappa = \frac{1}{4}(\partial\bar{\partial} + \bar{\partial}\partial)\tilde{\Psi} \quad (5)$$

and

$$\gamma = \gamma_1 + i\gamma_2 = \frac{1}{2}\partial\bar{\partial}\tilde{\Psi}, \quad (6)$$

where  $\tilde{\partial}$  and  $\bar{\partial}$  are the spin-raising and spin-lowering differential operators (see e.g. [Castro et al. \(2005\)](#) for details).

An arbitrary spin- $s$  function  $f$  on the sphere may be represented in the basis of spin- $s$  spherical harmonic functions  ${}_sY_{\ell m}$ :

$$f(\hat{n}) = \sum_{\ell m} f_{\ell m} {}_sY_{\ell m}(\hat{n}) \quad (7)$$

where

$$f_{\ell m} = \int d\Omega f(\hat{n}) {}_sY_{\ell m}^*(\hat{n}). \quad (8)$$

In this basis Eqs. (5) and (6) become

$$\kappa_{\ell m} = -\frac{1}{2}\ell(\ell+1)\tilde{\Psi}_{\ell m} \quad \text{and} \quad (9)$$

$$\gamma_{\ell m} = \frac{1}{2}\sqrt{(\ell-1)\ell(\ell+1)(\ell+2)}\tilde{\Psi}_{\ell m}, \quad (10)$$

respectively, and hence

$$\gamma_{\ell m} = -\sqrt{\frac{(\ell-1)(\ell+2)}{\ell(\ell+1)}}\kappa_{\ell m}. \quad (11)$$

The shear field may also be decomposed into  $E$ - and  $B$ -modes, with coefficients

$$E_{\ell m} = -\frac{1}{2} \int d\Omega [\gamma(\hat{n}) {}_{+2}Y_{\ell m}^*(\hat{n}) + \gamma^*(\hat{n}) {}_{-2}Y_{\ell m}^*(\hat{n})] \quad (12)$$

and

$$B_{\ell m} = \frac{i}{2} \int d\Omega [\gamma(\hat{n}) {}_{+2}Y_{\ell m}^*(\hat{n}) - \gamma^*(\hat{n}) {}_{-2}Y_{\ell m}^*(\hat{n})]. \quad (13)$$

The integrals are taken over the full sphere. The advantage of this decomposition is that to a good approximation, cosmic shear produces only  $E$ -modes (e.g. [Schneider 2005](#); [Bartelmann & Maturi 2017](#)), and the presence of  $B$ -modes can indicate systematic errors in the data (e.g. [Heymans et al. 2006](#); [Asgari et al. 2019](#)). These definitions use the  $H = 1$  sign convention (in the notation of [Lewis \(2005\)](#)), as is appropriate for HEALPIX; one consequence is that  $\gamma = -(E + iB)$ .

Galaxy surveys directly observe neither shear nor convergence, observing instead galaxy shape ellipticities  $\epsilon$  (and optionally sizes and/or fluxes). These shapes are noisy estimates of the shear field in the weak lensing regime ( $\kappa \ll 1$ ). In this regime one has, for a large number of galaxies,  $\langle \epsilon \rangle \approx \gamma/(1 - \kappa) \approx \gamma$ . Both shape noise (due to the random intrinsic shapes of galaxies) and measurement noise (a smaller effect than shape noise) are taken into account in the standard deviation  $\sigma_\epsilon$  of the distribution of the ellipticities; this distribution is usually assumed to be approximately gaussian for a sufficiently large area density of sources ([Joachimi & Bridle 2010](#); [Van Waerbeke et al. 2013](#); [Alsing et al. 2016](#); [Chang et al. 2018](#)). Intrinsic alignments can also introduce correlations of ellipticities (e.g., [Heavens et al. 2000](#); [Catelan et al. 2001](#); [Kirk et al. 2015](#); [Kiessling et al. 2015](#); [Joachimi et al. 2015](#); [Blazek et al. 2015](#)), and this effect will be included in the inferred power spectra.

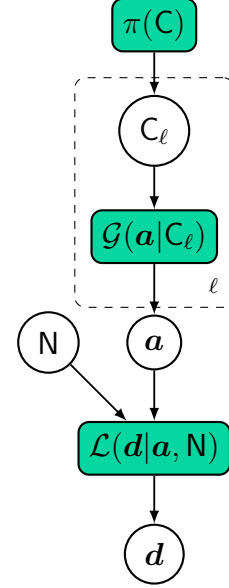


FIG. 1.—: Directed acyclic graph representing the Bayesian hierarchical model in Eq. (14) for maps and angular power spectra inference. Begin by drawing the angular power spectra  $C_\ell$  from a prior distribution  $\Pi(C_\ell)$ . Then draw a set of spherical harmonics coefficients for the shear fields  $\mathbf{a}$ , conditional upon the angular power spectra. Finally draw a set of noisy tomographic cosmic shear fields given the signal,  $\mathbf{a}$ , and the noise covariance,  $\mathbf{N}$ , based on the realisations from the previous steps.

### 3. THE POSTERIOR AND HMC SAMPLING

#### 3.1. Joint posterior of fields and their covariance

The posterior from which we draw samples consists of the full sky maps in harmonic space  $\mathbf{a}$  and their power spectra  $\mathbf{C}$ , given the data  $\mathbf{d}$  and the noise covariance  $\mathbf{N}$ . Fig. 1 shows a directed acyclic graph for the model presented in this section. Here  $\mathbf{a}$  and  $\mathbf{d}$  are concatenations of the spherical harmonic coefficients and the field values from different tomographic bins into a single map parameter vector and a single data vector. The power spectrum  $\mathbf{C}$  contains auto- and cross-power spectra across tomographic bins, with  $E$ - and  $B$ -mode correlations, as well as the parity-violating  $EB$ -mode cross-correlations. For more details, see the companion paper (Sellentin, Loureiro et al., *in prep*). The posterior is

$$\mathcal{P}(\mathbf{C}, \mathbf{a} | \mathbf{d}, \mathbf{N}) \propto \mathcal{L}(\mathbf{d} | \mathbf{a}, \mathbf{N}) \mathcal{G}(\mathbf{a} | \mathbf{C}) \pi(\mathbf{C}). \quad (14)$$

The first factor is the probability at field level:

$$\mathcal{L}(\mathbf{d} | \mathbf{a}, \mathbf{N}) \propto \exp \left[ -\frac{1}{2} (\mathbf{d} - \mathbf{Y}\mathbf{a})^T \mathbf{N}^{-1} (\mathbf{d} - \mathbf{Y}\mathbf{a}) \right]. \quad (15)$$

The second factor assumes a gaussian prior for the spherical harmonic coefficients:

$$\mathcal{G}(\mathbf{a} | \mathbf{C}) = \frac{1}{\sqrt{|2\pi\mathbf{C}|}} \exp \left( -\frac{1}{2} \mathbf{a}^T \mathbf{C}^{-1} \mathbf{a} \right). \quad (16)$$

This factor merits some discussion. The aim of the method is to infer the power spectra and the maps in a cosmology-independent way, making no assumptions about the gravity model. Thus, in contrast to BORG-

WL (Porqueres et al. 2021, 2022), we do not sample the initial gaussian field and then forward model. Instead, we want the least informative prior for the coefficients, for a given power spectrum, with no reliance on a model-dependent knowledge (in principle) of the statistics of the shear fields. This least informative, maximum-entropy prior is a gaussian (Jaynes 2003), which ensures that we are not using any model-dependent information. This does not imply that the fields themselves are realisations of a zero-mean gaussian with isotropic covariance, nor that a map created from the spherical harmonic coefficients of a given posterior sample is a realisation of such a process, since these are conditioned on the data. This is similar to the known behaviour of Wiener filters: where the data are highly constraining, the posterior will have small variance around the data, but where they are noisy, the variance will be dominated by the prior information about the signal.

The last factor in the posterior is a prior on the angular power spectra. We choose a power of the determinant

$$\pi(C) = |C|^q \quad (17)$$

with  $q = 0$  in the standard implementation. In contrast, the Jeffreys prior corresponds to  $q = -(N_p + 1)/2$  (where  $C_\ell$  has  $N_p \times N_p$  entries), as discussed in Sellentin & Heavens (2016); a frequency-matching choice of  $q$  can also be made (Percival et al. 2022) if desired. We set the prior to zero outside the set of positive definite matrices.

### 3.2. Hamiltonian Monte Carlo

Our aim is to infer the denoised maps and power spectra from simulated input data, using the Bayesian hierarchical model depicted in Fig. 1. Only a few samplers can handle such a high-dimensional parameter space. Gibbs sampling (Geman & Geman 1984; Casella & George 1992) as used by Wandelt et al. (2004); Eriksen et al. (2004); Larson et al. (2007); Alsing et al. (2016, 2017); Colombo et al. (2022) can generate samples using the conditional distributions  $\mathcal{P}(\mathbf{a}|C, \mathbf{d})$  and  $\mathcal{P}(C|\mathbf{a}, \mathbf{d})$ ; however, this method is probably too inefficient to sample the full posterior distribution in Eq. (14) for upcoming weak lensing analyses.

Instead, we take an approach similar to that used by most field-level inference works (Jasche & Kitaura 2010; Jasche & Wandelt 2013; Leclercq et al. 2015; Jasche & Lavaux 2019; Porqueres et al. 2021, 2022): we implement a tuned version of the HMC algorithm. This section outlines the key details; see the ALMANAC core paper (Sellentin, Loureiro et al., *in prep*) for more information.

In HMC (Hanson 2001; Hajian 2007; Neal 2011) we view the negative logarithm of the posterior density as a potential energy

$$\psi(\mathbf{a}, C|\mathbf{d}) = -\ln \mathcal{P}(\mathbf{a}, C|\mathbf{d}). \quad (18)$$

We then augment the parameter space with momentum variables drawn from a gaussian distribution, whose negative logarithm can be viewed as kinetic energy. A Hamiltonian trajectory of the resulting dynamical system is then computed using a leapfrog integrator. At the end of a trajectory, a Metropolis-Hastings step (Metropolis et al. 1953; Hastings 1970) decides if the trajectory is accepted (this corrects for any non-conservation of energy by the leapfrog integrator). If it is accepted, the

new sample is the trajectory’s end point; if it is rejected, the new sample is the trajectory’s start point. In either case, the momenta are resampled and another trajectory is computed (starting at the new sample). By iteration, the sampler builds up a Monte Carlo Markov Chain.

Step sizes and other parameters of the leapfrog integrator must be carefully tuned; see the companion paper (Sellentin, Loureiro et al., *in prep*) for details of this tuning. The sampling is challenging, since the shape of the posterior in the  $\mathbf{a} \times C$  plane exhibits a ‘stingray’ geometry (Neal 2000; Betancourt & Girolami 2013) that results in large correlation lengths and slow convergence; a reparametrisation of the parameter space, as discussed in the following section, can improve convergence.

### 4. CHOLESKY DECOMPOSITION COORDINATES

The particular challenge of tomographic weak lensing is that the covariance matrix, although block-diagonal in  $\ell$  and  $m$ , is dense for the  $E$  and  $B$  correlations across  $N_b$  tomographic bins. Thus there are dense sub-block matrices of size  $2N_b \times 2N_b$ , with strong correlations between neighbouring bins. We cannot straightforwardly sample the elements of  $C$  since the HMC random walk can easily wander out of the subset of positive-definite matrices. To handle this we instead explored sampling either a) the matrix logarithm  $G$  (where  $C = \exp(G)$ ) or b) the ‘diagonal-log’  $K$  (see Eq. 21) of the Cholesky factor  $L$  (where  $C = LL^T$  with  $L$  lower-triangular) of the covariance matrix. Figure 2 shows, for a toy example, the geometry of the potential (the negative of the logarithm of the posterior density) using both parameterisations. For the strong correlations inherent in cosmic shear, the Cholesky decomposition was found to lead to chains with shorter correlation lengths (indeed, the matrix log formalism failed badly for this application). See below for further details of the Cholesky reparametrisation here.

When parameterising using  $\mathbf{a}$  and  $G = \ln(C)$  the posterior density has the following extreme shape. Set  $\mathbf{a}$  to zero, and let  $G$  be strongly negative (corresponding to  $C$  close to zero); at such points there is poor agreement between  $\mathbf{a}$  and the data (this reduces the posterior density) but excellent agreement between  $\mathbf{a}$  and  $C$  (this increases the posterior density). But the former factor is bounded, while the latter factor becomes arbitrarily large as  $G$  goes to negative infinity. Thus the posterior density is unbounded; there is no peak. However when  $C$  is small the posterior density falls off very quickly when the  $\mathbf{a}$  move away from zero. Thus in the coordinates  $\mathbf{a}$  and  $G = \ln(C)$  the posterior density shape will resemble a funnel, or a stingray (Fig. 2a). Such an extreme shape is difficult to sample from using an HMC sampler. A remedy can be to reparameterise, in order to avoid the occurrence of the stingray (or, as we do, to move it to a less bothersome location in parameter space). For alternative approaches, see (Jewell et al. 2009; Racine et al. 2016).

In an analysis of a single  $a_{\ell m}$  and a single  $C_\ell$ , the ratio  $x = a_{\ell m}/\sqrt{C_\ell}$  will always be of unit variance. Therefore, although it may not solve all problems, it can avoid the occurrence of a stingray. As we analyze many multipoles and power spectra jointly, the multivariate analogue is to flatten all  $a_{\ell m}$  modes of the same  $\ell$  jointly. This can be achieved by Cholesky decomposing their covariance matrix  $C_\ell$ .



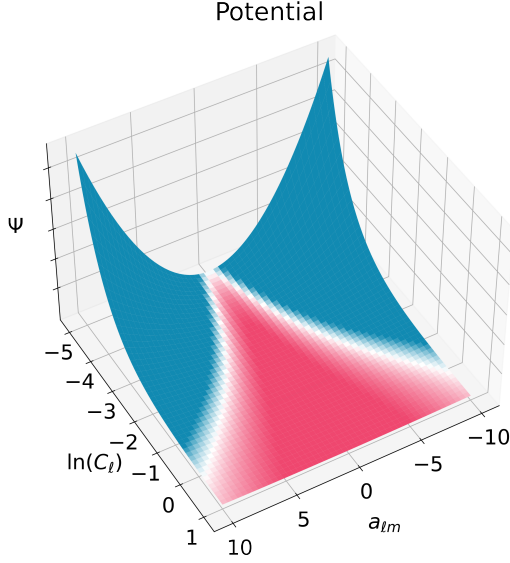
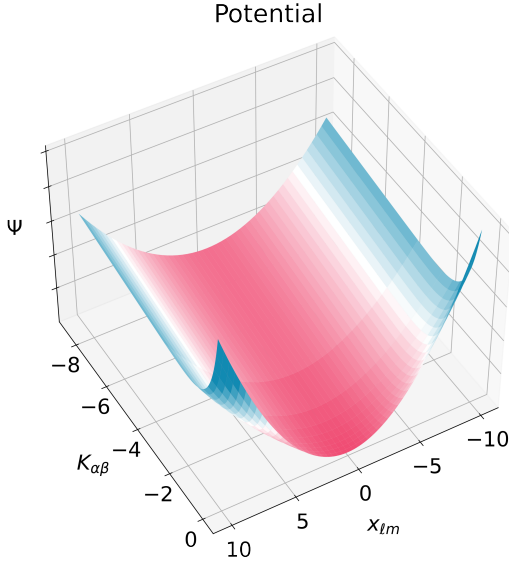
(a) Matrix-log parameters,  $\{\mathbf{a}, \mathbf{G}\}$ (b) Cholesky decomposition parameters,  $\{\mathbf{x}, \mathbf{K}\}$ 

FIG. 2.—: A toy example illustrating the geometry of the potential density in (a) the matrix-log parameterisation  $\{\mathbf{a}, \mathbf{G}\}$  and in (b) the Cholesky decomposition parameterisation  $\{\mathbf{x}, \mathbf{K}\}$ . This toy example shows a slice in the map  $\times$  angular power spectra dimensions for the negative log-posterior (potential) illustrated by the DAG in Fig. 1 using different coordinate systems. The potential density varies from low (pink) to high (blue) and values have been omitted since the normalisation is arbitrary. The matrix-log parameterisation has a stingray shape, also known as Neal's Funnel (Neal 2000); this posterior shape is known to be difficult to sample from.

In the rest of this section we fix  $\ell$  (between  $\ell_{\min}$  and  $\ell_{\max}$ ) and for notational simplicity we drop the dependence on  $\ell$  (so for example  $\mathbf{a}$  now refers to  $a_{\ell m}$  for varying  $m$  and this fixed  $\ell$ , while  $\mathbf{C}$  refers to what was previously called  $\mathbf{C}_\ell$ ).

Each matrix  $\mathbf{C}$  is relatively small (for example, dimension 3 for a CMB  $TEB$ -analysis, and dimension  $2N_b$  for a cosmic shear analysis with  $N_b$  redshift bins and both  $E$ - and  $B$ -modes) and hence can be decomposed at reasonable numerical cost.

For positive definite  $\mathbf{C}$  the Cholesky factor  $\mathbf{L}$  is the unique lower-triangular matrix with positive elements on the diagonal satisfying  $\mathbf{C} = \mathbf{L}\mathbf{L}^T$ . Given  $\mathbf{a}$  define  $\mathbf{x}$  via

$$\mathbf{x} = \mathbf{L}^{-1}\mathbf{a}; \quad (19)$$

then if  $\mathbf{a}$  has mean zero and covariance  $\mathbf{C}$  then  $\mathbf{x}$  will have mean zero and unit covariance

$$\langle \mathbf{x}\mathbf{x}^T \rangle = \mathbb{I}. \quad (20)$$

We define the *diagonal-log*  $\mathbf{K}$  of  $\mathbf{L}$  to be

$$K_{\alpha\beta} = \begin{cases} \ln(L_{\alpha\beta}) & \text{if } \alpha = \beta, \\ L_{\alpha\beta} & \text{otherwise.} \end{cases} \quad (21)$$

Then  $\{\mathbf{x}, \mathbf{K}\}$  provides an alternative parameterisation of  $\{\mathbf{a}, \mathbf{C}\}$ ; note that an arbitrary  $\mathbf{K}$  will generate a positive-definite  $\mathbf{C}$ .

#### 4.1. Jacobian for Cholesky coordinates

Reparameterising from  $\{\mathbf{a}, \mathbf{C}\}$  to  $\{\mathbf{x}, \mathbf{K}\}$  introduces a Jacobian factor in the posterior density. Now

$$p(\mathbf{x}, \mathbf{K}) d\mathbf{x} d\mathbf{K} = p(\mathbf{a}, \mathbf{C}) d\mathbf{a} d\mathbf{C} \quad (22)$$

and so the Jacobian factor is

$$|\mathbf{J}| = \left| \frac{\partial \mathbf{a} / \partial \mathbf{x}}{\partial \mathbf{C} / \partial \mathbf{x}} \frac{\partial \mathbf{a} / \partial \mathbf{K}}{\partial \mathbf{C} / \partial \mathbf{K}} \right| = |\partial \mathbf{a} / \partial \mathbf{x}| |\partial \mathbf{C} / \partial \mathbf{K}|; \quad (23)$$

the second equality follows from  $\partial \mathbf{C} / \partial \mathbf{x} = 0$  (since it is evaluated at constant  $\mathbf{K}$ ). We have  $\mathbf{a} = \mathbf{L}\mathbf{x}$  and so

$$|\partial \mathbf{a} / \partial \mathbf{x}| = |\mathbf{L}| = \prod_{\alpha=1}^n L_{\alpha\alpha}. \quad (24)$$

The determinant of the transformation from  $\mathbf{C}$  to  $\mathbf{L}$  is (Gupta 1999):

$$|\partial \mathbf{C} / \partial \mathbf{L}| = 2^n \prod_{\alpha=1}^n L_{\alpha\alpha}^{n+1-\alpha}, \quad (25)$$

while

$$|\partial \mathbf{L} / \partial \mathbf{K}| = \prod_{\alpha=1}^n \frac{\partial L_{\alpha\alpha}}{\partial K_{\alpha\alpha}} = \prod_{\alpha=1}^n L_{\alpha\alpha}. \quad (26)$$

Combining these results yields

$$|\mathbf{J}| = 2^n \prod_{\alpha=1}^n L_{\alpha\alpha}^{n+3-\alpha} = 2^n \exp \left[ \sum_{\alpha=1}^n (n+3-\alpha) K_{\alpha\alpha} \right]. \quad (27)$$

#### 4.2. Negative Log Posterior in Cholesky coordinates

In Cholesky coordinates  $\{\mathbf{x}, \mathbf{K}\}$  the negative logarithm  $\psi$  of the posterior (Eq. (14)) becomes:

$$\psi(\mathbf{x}, \mathbf{K}) = \frac{1}{2}(\mathbf{d} - \mathbf{Y}\mathbf{L}\mathbf{x})^T \mathbf{N}^{-1}(\mathbf{d} - \mathbf{Y}\mathbf{L}\mathbf{x}) + \frac{\mathbf{x}^T \mathbf{x}}{2} + \sum_{\alpha=1}^n (\alpha - 2 - n - 2q) K_{\alpha\alpha} . \quad (28)$$

Here we have included the Jacobian term (Eq. (27)), we have used for example  $\mathbf{a} = \mathbf{L}\mathbf{x}$  and  $|\mathbf{C}| = |\mathbf{L}|^2$ , and we have silently dropped irrelevant additive constants. The final summand includes an implied sum over  $\ell$ .

This new coordinate system creates a posterior shape that can be explored more efficiently by a HMC sampler than the shape of the posterior in the  $\{\mathbf{a}, \ln(\mathbf{C})\}$  coordinates. The data products outputted by the sampler are transformed back to the usual  $\{\mathbf{a}, \mathbf{C}\}$ -parameters that a cosmologist would expect.

#### 4.3. Gradients in Cholesky coordinates

The HMC sampler requires for its leapfrog routine the derivatives of the potential (i.e. the negative logarithm of the posterior)  $\psi$  with respect to both  $\mathbf{x}$  and  $\mathbf{K}$  parameters. Straightforward calculations show that the derivative with respect to  $\mathbf{x}$  is

$$\frac{\partial \psi}{\partial x_\alpha} = -[\mathbf{L}^T \mathbf{Y}^T \mathbf{N}^{-1}(\mathbf{d} - \mathbf{Y}\mathbf{L}\mathbf{x})]_\alpha + x_\alpha \quad (29)$$

and that the derivative with respect to  $\mathbf{K}$  is

$$\begin{aligned} \frac{\partial \psi}{\partial K_{\alpha\beta}} = & \left( -(\delta_{\alpha\beta}^K (L_{\alpha\beta} - 1) + 1) \right. \\ & \times x_\beta [\mathbf{Y}^T \mathbf{N}^{-1}(\mathbf{d} - \mathbf{Y}\mathbf{L}\mathbf{x})]_\alpha \Big) \\ & + \delta_{\alpha\beta}^K (\alpha - 2 - n - 2q) ; \end{aligned} \quad (30)$$

here  $\delta^K$  is the Kronecker delta.

#### 4.4. Hessian in Cholesky coordinates

The Hessian of the posterior can be a good approximation for the mass matrix of an HMC sampler. If one does not want to (or cannot) use the full Hessian, one could still set the leapfrog step size to be the inverse square root of the diagonal of the Hessian; ALMANAC sets the initial step sizes in this way (although the step sizes are later tuned to better values). The diagonal elements of the Hessian are

$$\frac{\partial^2 \psi}{\partial x_\alpha \partial x_\alpha} = [\mathbf{L}^T \mathbf{Y}^T \mathbf{N}^{-1} \mathbf{Y} \mathbf{L}]_{\alpha\alpha} + 1 \quad (31)$$

and

$$\begin{aligned} \frac{\partial^2 \psi}{\partial K_{\alpha\beta} \partial K_{\alpha\beta}} = & (\delta_{\alpha\beta}^K (L_{\alpha\beta}^2 - 1) + 1) x_\beta^2 [\mathbf{Y}^T \mathbf{N}^{-1} \mathbf{Y}]_{\alpha\alpha} \\ & - \delta_{\alpha\beta}^K L_{\alpha\beta} x_\beta [\mathbf{Y}^T \mathbf{N}^{-1}(\mathbf{d} - \mathbf{Y}\mathbf{L}\mathbf{x})]_\alpha . \end{aligned} \quad (32)$$

We may estimate  $[\mathbf{Y}^T \mathbf{N}^{-1} \mathbf{Y}]_{\alpha\alpha}$  as follows: let  $\mathbf{y}$  be a normal random variable with zero mean and covariance  $\langle \mathbf{y} \mathbf{y}^T \rangle = \mathbf{N}^{-1}$ . Then observe that  $[\mathbf{Y}^T \mathbf{N}^{-1} \mathbf{Y}]_{\alpha\alpha}$  is the expected value of the square of  $[\mathbf{y}^T \mathbf{Y}]_\alpha$ ; this latter quantity may be estimated using Monte-Carlo style draws of

$\mathbf{y}$ . This technique allows us to calculate Eq. 31 and the first term in Eq. 32; however, the second term in Eq. 32 is challenging to calculate efficiently and we therefore estimate it by numerical differentiation.

#### 4.5. Reduced shear

The quantity that controls the shape distortion is not strictly the shear, but rather the reduced shear (e.g. Bartelmann & Maturi 2017),  $\gamma/(1 - \kappa)$ . For the tests in this paper we have not included reduced shear. In the future we intend to include reduced shear in the posterior calculation. This will complicate the calculation of the derivatives and we propose not including reduced shear in the derivatives calculation. The small (percent-level) errors in the resulting trajectories will then be dealt with completely by the Metropolis-Hastings acceptance/rejection step, which also deals with inaccuracies in the leapfrog integrator.

### 5. SIMULATION

In order to demonstrate ALMANAC's application to the next generation of cosmic shear experiments, we used gaussian random fields (GRF, Bardeen et al. 1986; Hoffman & Ribak 1992) to simulate a Euclid-like cosmic shear survey. Euclid is an excellent showcase for ALMANAC's performance and application due to sky coverage, complex mask geometry, and expected data quality. Since ALMANAC infers all scales available from a given multipole range to properly forward-model the underlying field, galaxy surveys with large sky coverage such as Euclid and LSST are ideal data sets for the methodology described in this work.

The Euclid photometric sample will likely be divided into ten redshift tomographic bins with an equal effective galaxy number density of  $\bar{n} = 3$  galaxies/arcmin<sup>2</sup> for each bin (Laureijs et al. 2011; Euclid Collaboration et al. 2020; Tutusaus et al. 2020; Taylor et al. 2021; Euclid Collaboration et al. 2022). We arbitrarily select two of these ten tomographic bins to define the weak lensing tracers for the underlying theoretical angular power spectra. The fiducial  $C_\ell$  for the  $E$ -modes used in the simulation were calculated using CCL (Chisari et al. 2019) with a Planck 2018 fiducial cosmology (Planck Collaboration et al. 2020)<sup>1</sup>, in a range between  $\ell_{\min} = 4$  and  $\ell_{\max} = 2048$ . Meanwhile, the  $B$ -mode power spectra were set to  $10^{-15}$  and the  $C_\ell^{E_i B_j}$  were set to  $10^{-20}$ , both constant across the multipole range used for the  $E$ -mode power spectra.

The survey angular geometry mask was created by masking out the galactic plane and the ecliptic based on the description in Euclid Collaboration et al. (2022). We then randomly masked pixels using a Poisson distribution to mimic the effects of stars in the field. The resulting mask is shown in the bottom left of Fig. 3.

The last element in the simulation is shape noise, taken to be  $\sigma_\epsilon = 0.28$ . Note (see Fig. 3) that the  $B$ -modes are almost six orders of magnitude below the noise power spectra.

The noise covariance in real (pixel) space  $\mathbf{N}$  is taken to be a diagonal matrix. It has  $2N_b N_{\text{pix}}$  diagonal elements

<sup>1</sup>  $\Omega_{\text{cdm}} = 0.27$ ;  $\Omega_b = 0.045$ ;  $\Omega_k = 0$ ;  $n_s = 0.96$ ;  $\sigma_8 = 0.83$ ;  $h = 0.67$ .

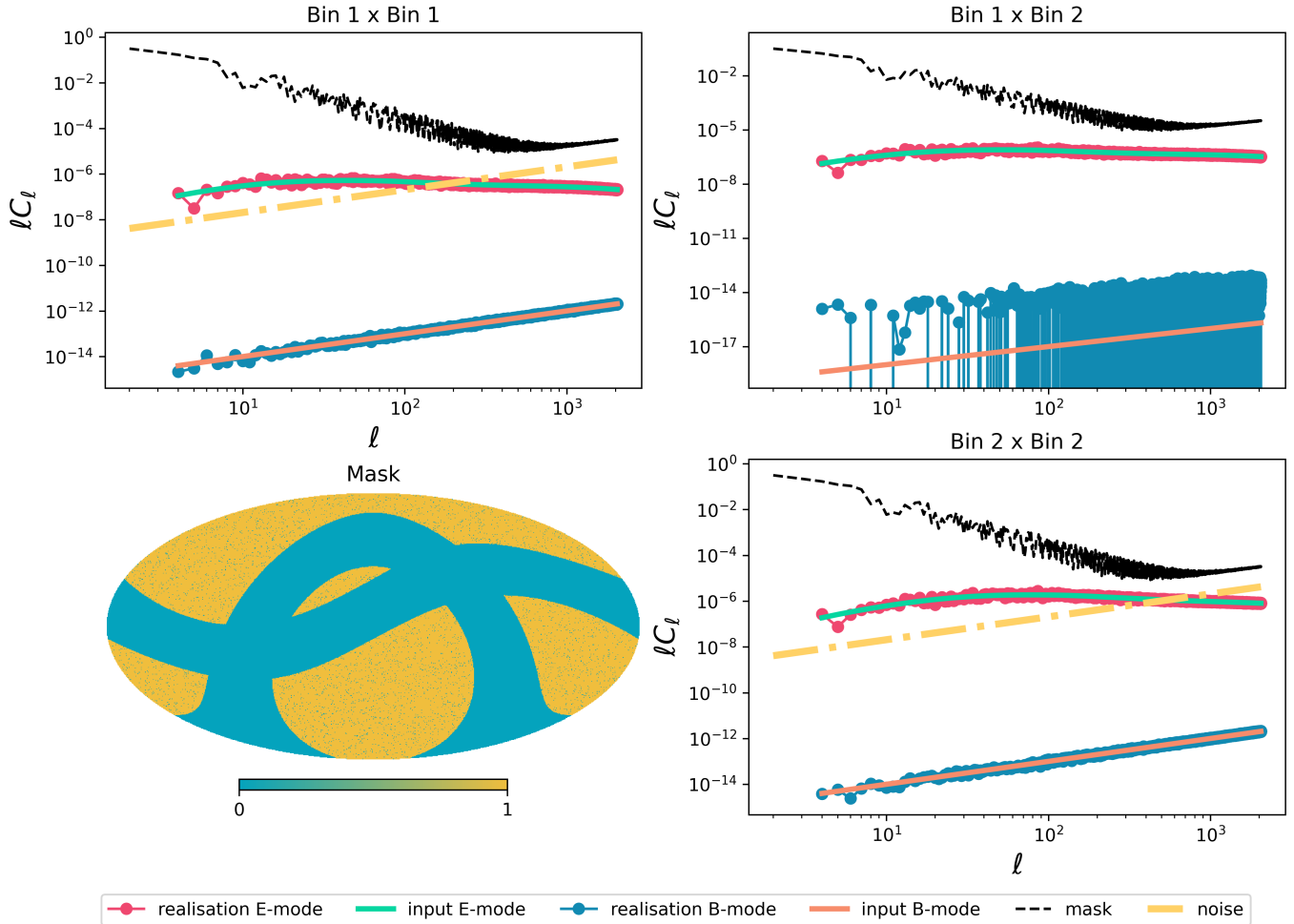


FIG. 3.— Setup for the Euclid-like cosmic shear survey simulation, showing the input angular power spectra to the GRF simulation for the  $E$ -modes (green line) and  $B$ -modes (orange line), the mask angular power spectra (dashed black line), the noise power spectra (yellow dot-dashed line), and the data realisation angular power spectra for  $E$ - and  $B$ -modes (pink and blue dots, respectively). The bottom left figure shows the angular mask used in the simulation.

(the factor of 2 corresponding to the two components of shear); for a given shear component, tomographic bin  $i$ , and pixel  $p$  the corresponding entry in  $\mathbf{N}$  is  $\sigma_\epsilon^2/(2\bar{n}_i)$  if  $p$  is unmasked and infinity otherwise. Here  $\bar{n}_i$  is the lensing source number per pixel in bin  $i$ .

The simulations are performed using a HEALPIX (Gorski et al. 1999) resolution of  $N_{\text{side}} = 1024$  ( $\Delta\Omega_{\text{pix}} = 11.8 \text{ arcmin}^2$ ) by sampling correlated  $\mathbf{a}$  from a multivariate gaussian distribution,  $\mathbf{a} \sim \mathcal{N}(0; \mathbf{C}_\ell)$ , and then transforming the signal maps into real space. Next, using the aforementioned galaxy density and shape noise, we add gaussian noise to the signal maps with a variance of  $\sigma^2 = \sigma_\epsilon^2/(2\bar{n}_i)$  per component. In a final step, we apply the mask shown in Fig. 3 to all the galaxy ellipticity data maps.

Although a more realistic N-body simulation with ray-tracing would include higher-order effects into the tests, a GRF simulation allows for more control over the quantities we are probing and testing. It lets us quickly simulate correlated tomographic cosmic shear data, allowing full control and understanding of the effect of signal, noise, and mask; a GRF is the most reliable way to have full control of the simulation’s underlying angular

power spectrum and noise. This approach also allows us to keep fixed the simulation’s signal realisation while turning off shape noise and mask effects to produce the ground truth. More complex simulations would not pose any difficulties for the ALMANAC analysis presented in Sec. 6 as the method makes no assumptions on the input data maps beyond the spin and noise, and statistical isotropy.

## 6. RESULTS

We apply the ALMANAC BHM described in Sec. 3 to the Euclid-like simulation described in Sec. 5 probing a multipole range  $4 \leq \ell \leq 2048$  with  $N_{\text{side}} = 1024$ . Here we describe the main outputs from this analysis: the marginalised angular power spectrum and the inferred shear and convergence full sky maps. We further demonstrate other benefits of having the full joint posteriors of maps and angular power spectra, and we discuss implications for future cosmic shear surveys (such as our approach to  $EB$  leakage, and the recovery of large scale modes).

We keep the  $B$ -mode auto-power spectra in the modelling, with a small signal amplitude in the simulated data; although in the standard model of cosmology these

modes are expected to be negligible for cosmic shear, we want the ability to detect systematic contamination that could appear through the  $B$ -modes (Heymans et al. 2006; Asgari et al. 2019).

The full posterior contains all the spin-2 spherical harmonics for both redshift tomographic bins and their angular power spectra; this results in a total of 16,813,990 dimensions (of which only 20,450 are for the angular power spectra,  $C_\ell$ ).

We ran two simultaneous chains using different starting points and different random seeds. Each chain contains  $N_{\text{samples}} \approx 2.25 \times 10^5$  samples (after burn-in and tuning) and each had an acceptance ratio of  $\sim 86\%$ . For both chains we used  $N_{\text{tune}} = 2 \times 10^4$  and  $N_{\text{if-tune}} = 5 \times 10^3$  samples to perform the step-size tuning described in Sella et al., in *prep*. Unless stated otherwise, all the results presented in this section come from combining the chains (once the chains were individually converged – see Sec. 6.3 for a discussion of the convergence diagnostics for chains used in this analysis).

### 6.1. Inferred Angular Power Spectra

For each element of the power spectra we calculate its one-dimensional marginalised posterior, together with the mode and the 68.3% and 95% credible intervals (C.I.) of this marginalised posterior. The results are shown in Fig. 4 for the  $E$ - and  $B$ -modes in both tomographic bins and in Fig. 5 for the parity violating modes.

It is the *mode* of the marginalised posterior that we display in Figs 4 and 5; this choice is motivated by the non-gaussian nature of the marginalised posteriors for low- $\ell$  modes, as shown in Fig. 6. Here, taking the mean of the samples would be a biased estimate for the peak of the marginalised posteriors on large scales. We also stress that point estimates are not the purpose of this analysis; instead, we are interested in the full joint posterior of angular power spectra and full sky maps in harmonic space. Therefore, one should interpret Figs. 4 and 5 as lower-dimensional visualisations of a multidimensional space.

Fig. 4 demonstrates ALMANAC’s ability to infer the underlying angular power spectrum for cosmic shear data on the sphere up to scales relevant for the current and next generation of surveys. Although not a requirement for a Bayesian analysis, the marginalised  $E$ -mode  $C_\ell$ s agree well with the input power spectra given to the Euclid-like simulations within the 68.3% C.I. for all multipoles in the analysed range, including the largest scales available in the simulation. Our prior for  $C$  excludes non-positive-definite matrices, and hence all diagonal elements of  $C$  must be positive; in particular, the  $B$ -mode auto-power spectra cannot be zero or negative. The posterior in this case peaks at zero, and the samples may be used to set an upper bound for the  $B$ -mode power. Both the  $B$ -mode upper bound and the parity-violating modes are efficient probes for systematic contamination that can be calculated in a fully Bayesian way with the measurements produced by ALMANAC.

Fig. 6 shows several examples of marginalised one-dimensional posterior distributions of  $E$ -mode multipoles. This plot illustrates that the method can properly infer scales that would usually be considered too large (given the fraction of the sky made available by the survey’s mask), since the data in the unmasked regions, in

conjunction with the prior, constrain modes on all scales.

A particular issue when using point estimators of two-point statistics for weak lensing data is the occurrence of ambiguous modes due to the survey’s mask and anisotropic noise. Commonly referred to as ‘ $EB$  leakage’ (Bunn et al. 2003; Bunn 2008; Leistedt et al. 2017; Liu et al. 2019; Nicola et al. 2021), this effect causes high (low)  $B$ -modes to be confused with low (high)  $E$ -modes, yielding a negative correlation between these modes on the marginalised posterior distribution for a given multipole. Since we are not working with estimators of the  $E$ - and  $B$ -mode power spectra, instead inferring the full posterior of the underlying whole sky fields and their angular power spectra, such leakage of power from  $E$  to  $B$  does not arise. What may generically happen is that the posterior samples of  $E$ - and  $B$ -modes are correlated. To check for this effect, we calculate the  $r$ -correlation factor for each pair of auto power spectra samples  $\{C_{\ell=L}^{E_i, E_i}, C_{\ell=L}^{B_i, B_i}\}$  for a given multipole  $L$ . The  $r$ -correlation factors for both tomographic bins are plotted in Fig. 7, which shows a rather small level of correlation. Although we find no significant correlations between  $E$ - and  $B$ -modes in our analysis, we outline here another advantage of a Bayesian approach. Since we have the full posterior of angular power spectra, modes that demonstrate significant correlation can be removed by marginalising. We highlight, however, that since the full posterior distribution is known, this marginalisation would only be necessary if one were to take point estimates of the marginalised individual modes of the  $E$ -mode angular power spectra.

### 6.2. Inferred Shear and Convergence Maps

We next consider the spherical harmonic coefficients; these make up the larger subset of the joint set of parameters. In this section we analyse the posterior samples when marginalised over the angular power spectra. For each  $\mathbf{a}$  sample in the chains, we make a spherical harmonic transformation, following the formalism stated in Sec. 2, to obtain real-space maps for shear and convergence. The  $\mathbf{a}$  samples are quite large, so to reduce file size (and hence increase speed) only one  $\mathbf{a}$  sample in 800 is saved; this thinning yields 577 samples across both chains.

The main results for the inferred shear and convergence maps and their uncertainties are shown in Fig. 8 (first bin) and Fig. 9 (second bin). In these figures, the data maps (first row) show the simulated galaxy ellipticities (here data is missing due to the survey geometry mask, and the maps contain shape noise according to the description in Sec. 5). The fiducial maps (second row) show the same simulated maps but without the shape noise and survey mask (i.e. they contain only the underlying cosmic shear signal). The mean maps (third row) and standard deviation maps (fourth row) are calculated from the statistics of the  $\mathbf{a}$  samples transformed into real space. Finally, the ‘typical’ convergence map (fifth row, left) has coefficients determined from the  $E$ -modes with the highest posterior probability (compare Eq. (11)) :

$$\kappa_{\ell m}^{\text{best}} = -\sqrt{\frac{\ell(\ell+1)}{(\ell-1)(\ell+2)}} E_{\ell m}^{\text{best}} \quad (33)$$



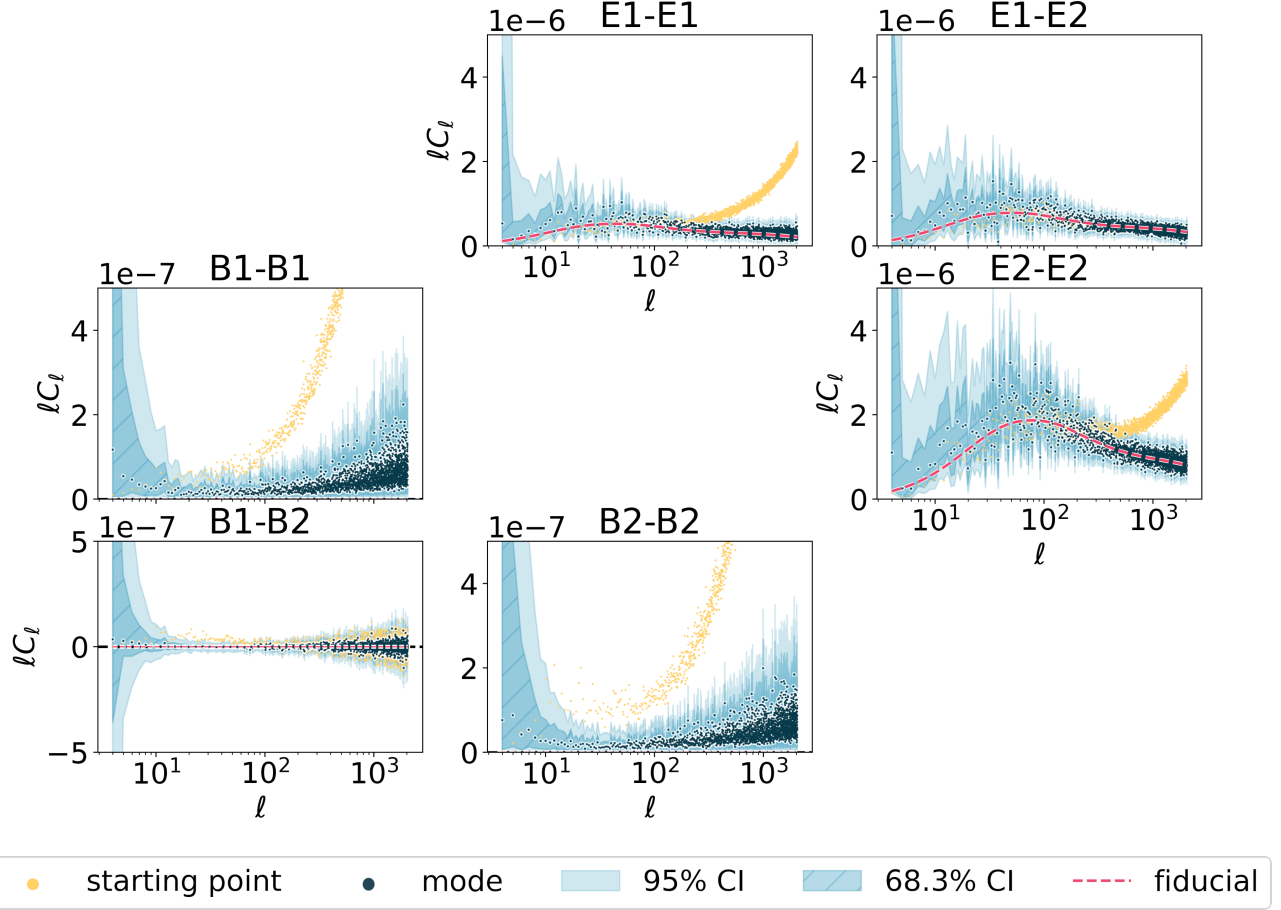


FIG. 4.—: Inferred marginalised angular power spectra for the  $E$ - and  $B$ -modes. Dark blue dots are the mode of the marginalised one-dimensional posterior for each multipole; the blue (resp. light blue) hashed area is the 68.3% (resp. 95%) C.I. The starting point for one of the chains is shown in yellow. The dashed red line is the ground truth given to the input simulation shown in Fig. 3. We stress that for the  $B$ -mode auto power spectra, ALMANAC can only set an upper bound (due to the prior on auto-correlations being positive and  $B$ -modes having an almost zero signal).

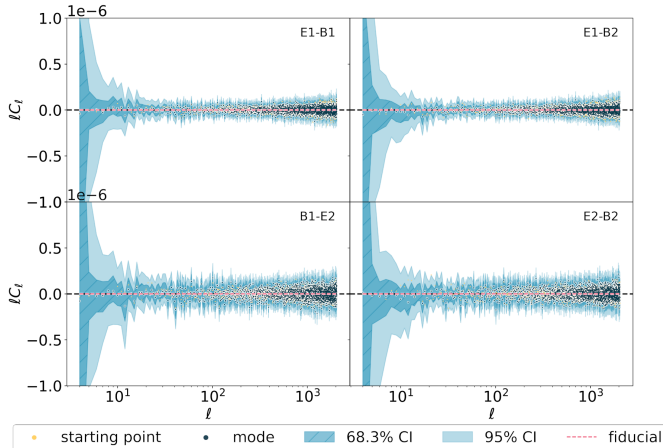


FIG. 5.—: Similar to Fig. 4 but showing the parity violating modes instead.

while the signed S/N ratio map (fifth row, right) is defined as

$$(S/N)_\kappa \equiv \frac{\kappa^{\text{best}}(\theta, \phi)}{\sigma_\kappa(\theta, \phi)} \quad (34)$$

where  $\sigma_\kappa$  is the standard deviation of the convergence maps at the relevant pixel. The typical map is generated from the  $\mathbf{a}$  in the sample that has the highest posterior probability. Given the high dimensionality of the parameter space, this sample is not to be considered an estimator of the peak of the posterior distribution; rather, it is simply to be considered as one specific representative point in the ‘typical set’ of the posterior (chosen in this way to reduce the chance of accidentally picking a sample from the tails). Note that neither the peak nor the mean will lie in the typical set.

Comparing the mean shear maps to the fiducial map, we see that ALMANAC samples can properly recover the underlying structure of shears where the input galaxy ellipticity maps have observations. For the masked areas, where observations are not present, the mean maps display suppression of structure for small scales. This is expected from the averaging of the samples. Each sample is characterized by a power spectrum that contains small-scale modes, so the sampled maps have fine structures even in the masked regions. However, in the masked regions, the small-scale structure is not well constrained, so different samples have different structures there, and these tend to average out when the mean map is computed. The masked regions also have higher posterior

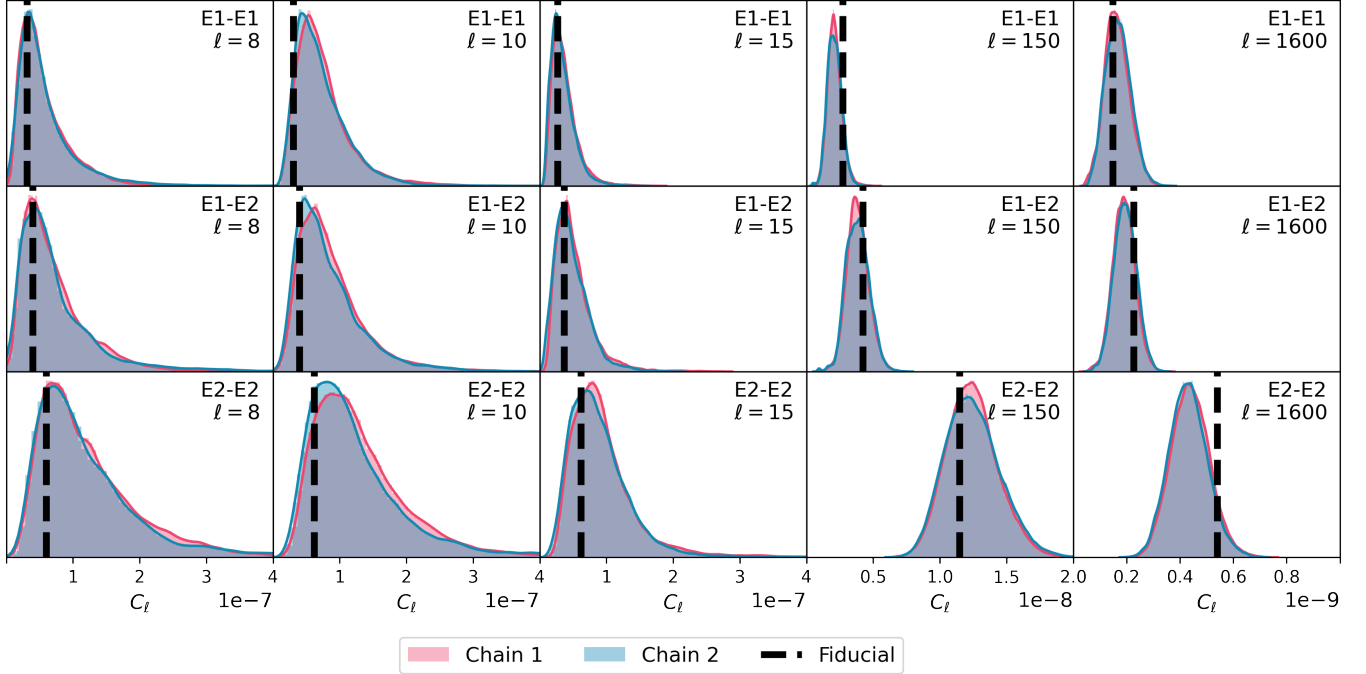


FIG. 6.—: Marginalised one-dimensional posterior distributions for  $E$ -modes of different multipoles ( $\ell = 8, 10, 15, 150, 1600$ ). As expected, marginalised posteriors for large scale modes are significantly non-gaussian while those for small scale modes are much closer to gaussian (due to the higher number of spherical harmonic coefficients available).

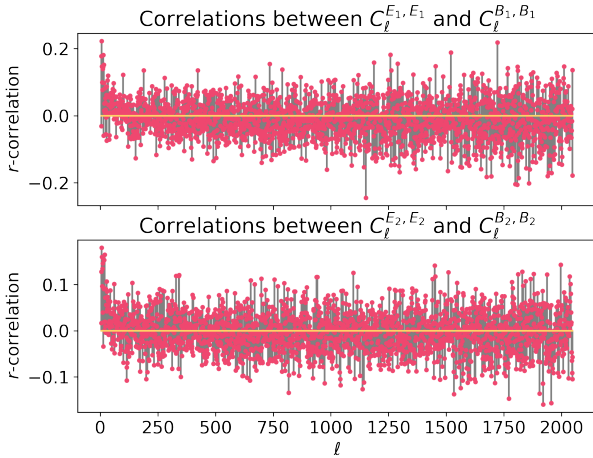


FIG. 7.—: Correlations between the samples of same multipoles between auto-power spectra of  $E$ - and  $B$ -modes. For each pair of  $C_\ell^{EE}$  and  $C_\ell^{BB}$  highly anti-correlated modes indicate that lower (higher)  $B$ -modes are degenerate with higher (lower)  $E$ -modes. We find no evidence for this effect in our analysis.

uncertainty, and this is reflected in the uncertainty maps shown in the fourth row of Figs. 8 and 9.

Finally, we can use Eqs. (9) and (10) to obtain typical maps for the tomographic projected lensing potential (or the projected Newtonian gravitational potential,  $\tilde{\Psi}$ , as defined by Eq. (2)) for the full sky. These maps are shown in Fig. 10, where they are compared to the ground-truth obtained from the fiducial simulations (same underlying signal as the data but full-sky and

noiseless). We overlay the mask (white semi-transparent region in the maps); this allows us to observe that ALMANAC's inferred gravitational field is in excellent agreement with fiducial field in unmasked regions, while, as expected, the inferred map displays an overall similar structure under the mask but with different locations of voids and walls than that found in the fiducial map.

We perform two main consistency checks in the recovered maps, one for the typical maps and another for the mean shear maps. The first test (see Fig. 11) compares the underlying signal realisation from the fiducial maskless and noiseless simulation with the pseudo- $C_\ell$  estimate of the typical shear maps. The results demonstrate that, if one is interested in a map that reflects the underlying two point statistics, a typical map is the correct quantity to use. As expected, the agreement between the two is better for the largest scales, while the typical map scatters around the fiducial value for the smaller scales (due to the missing information resulting from the mask). The second test (see Fig. 12) checks the distribution of residuals between the shear maps samples and the fiducial shear map

$$\mathcal{R}(\gamma_i) \equiv \frac{1}{\sigma_{\gamma_i}} (\bar{\gamma}_i - \gamma_i^{\text{fiducial}}) \quad (35)$$

where  $\bar{\gamma}_i$  is the mean map for the samples of shear component  $i$ ; these are expected to follow a standard normal distribution. The figure shows the distributions of the residuals for all recovered shear component maps, and a standard normal for comparison. The small difference seen for the lower redshift tomographic bins can be explained by their lower signal-to-noise affecting the ability of the method to accurately estimate these maps. How-

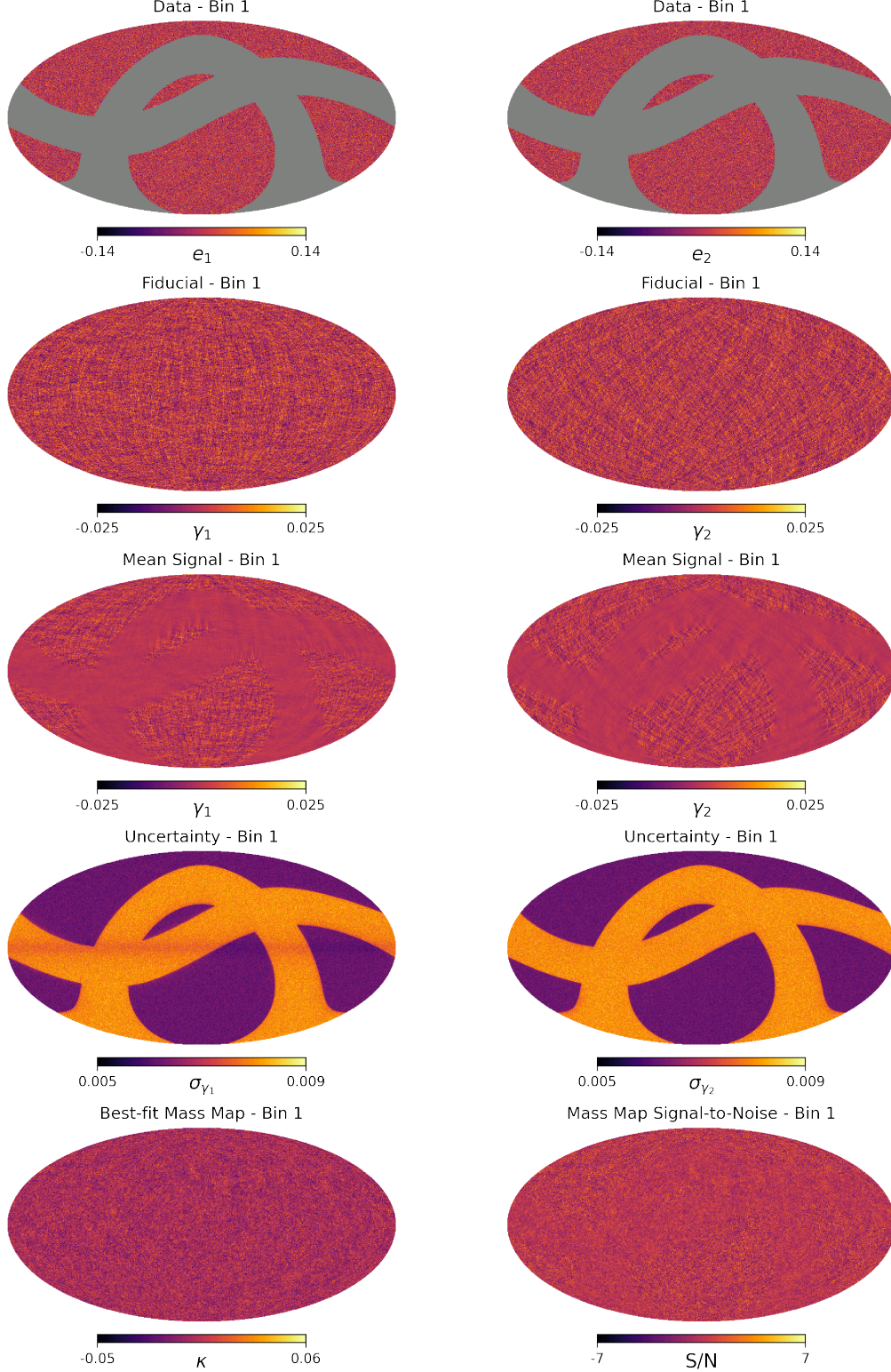


FIG. 8.—: Maps for the first redshift tomographic bin. Row 1: simulated galaxy ellipticity data; row 2: its underlying cosmic shear signal (fiducial); row 3: recovered mean shear components; row 4: errors for the components of the recovered shear; row 5: typical convergence (left) and its signed S/N ratio (right). The fiducial maps contain the same signal realisation as the simulated maps but without the shape noise and without the mask. The ‘typical’ maps are chosen to be the ones with the highest posterior probabilities in each of the thinned chains. The mean maps recovered most of the underlying structure shown in the fiducial maps in areas where data is present and are able to recover some of the large-scale information under the mask. The uncertainty on the recovered shear maps reflects the data missing due to the survey geometry.



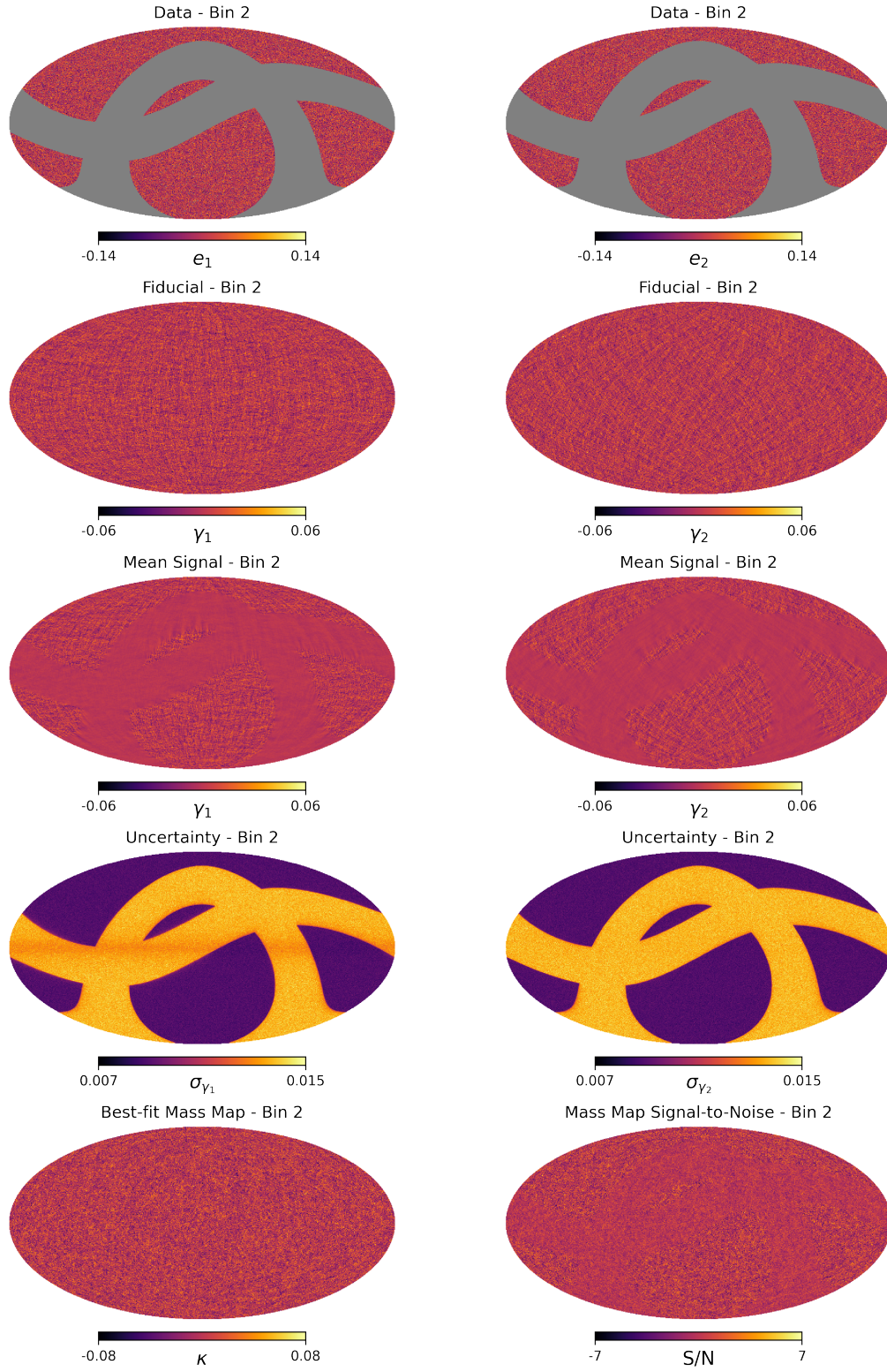


FIG. 9.—: Same as Fig. 8 but for the second tomographic bin.



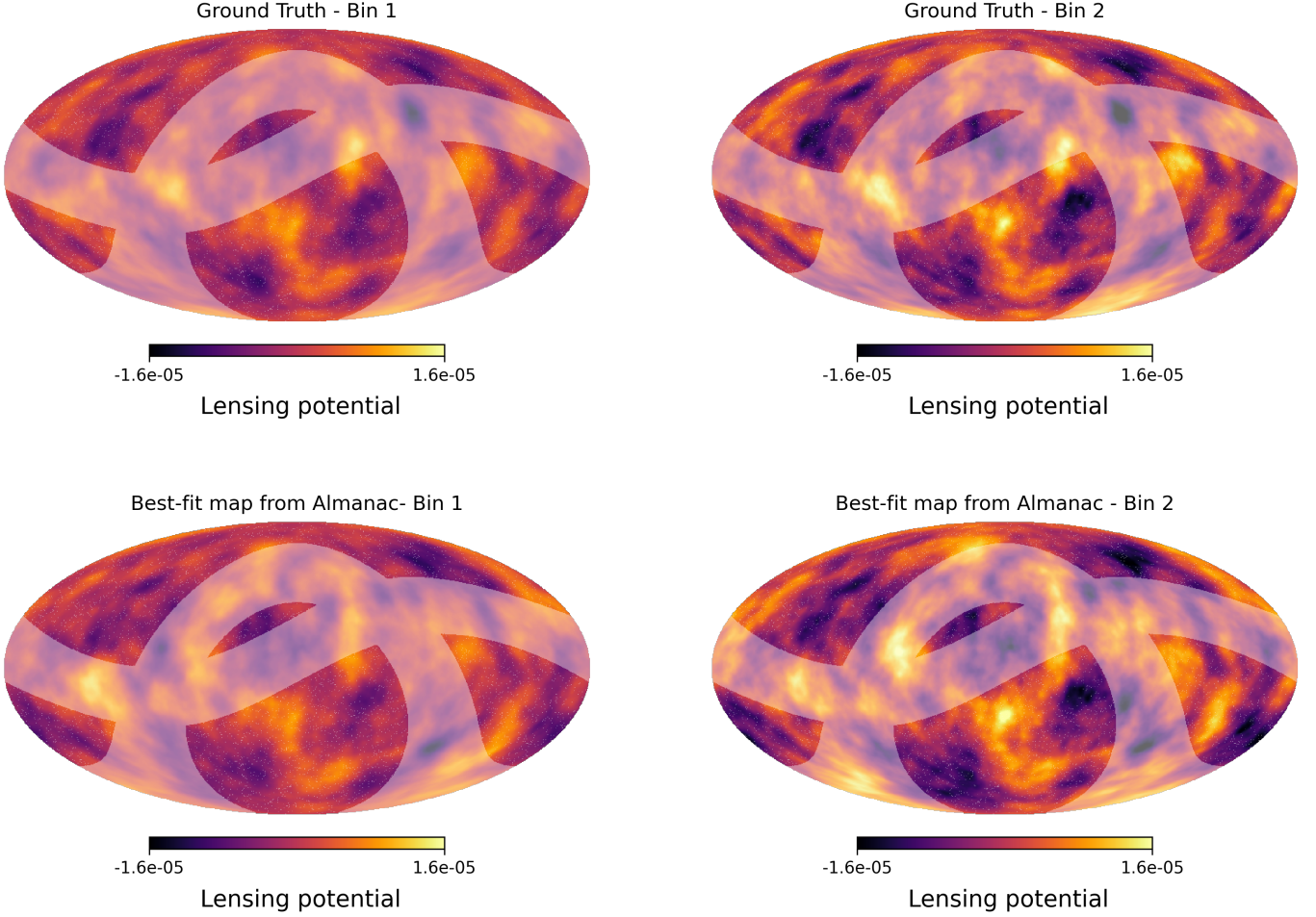


FIG. 10.—: Reconstructed projected gravitational potential (or lensing potential),  $\tilde{\Psi}(\hat{n})$ , from typical ALMANAC maps for both tomographic bins. Top: the ground-truth lensing potential obtained from the fiducial maskless noiseless simulations (second row on Fig. 8 and 9). Bottom: projected lensing potential reconstructed from the simulated data (first row on Fig. 8 and 9) using a typical ALMANAC map. Here, we overlay the mask used in the simulations for visualisation purposes.

ever, the difference is below one sigma and does not raise concerns about the recovered maps shown in Figs. 8 and 9.

### 6.3. Convergence diagnostics

In this section we describe the convergence diagnostics used to assess the validity of the chains (and hence the validity of the results shown in the previous sections). Assessing convergence of a high-dimensional Monte Carlo chain is a notoriously difficult problem. We examined several convergence diagnostics on the individual chains, probing different aspects of the convergence: a trace of the log posterior, the Fraction of Missing Information, the correlation length of the chains, Hanson’s statistic, and the Gelman-Rubin test. Further details are in Sellentin, Loureiro et al., *in prep.*

Fig. 13 shows the negative log posterior trace and its histogram for the combined chains. The trace (upper plot) shows no obvious correlations, and both chains show visually similar behaviour. This first test demonstrates that both chains are consistently probing the

same underlying distribution. The histogram of posterior values (bottom plot) also shows a well-behaved distribution, suggesting that burn-in was properly removed for both chains and that both chains burned-in to the same region of the underlying posterior.

As a second test, we calculate the Fraction of Missing Information (FMI; Betancourt 2016)<sup>2</sup>. This diagnostic assesses if the sampler is correctly exploring the full range of total energy submanifolds within phase space. It is defined as (Betancourt 2016, 2017)

$$\text{FMI} = \frac{\sum_{n=1}^N (E_n - E_{n-1})^2}{\sum_{n=0}^N (E_n - \bar{E})^2}, \quad (36)$$

where  $E_n$  is the total energy of the Hamiltonian system at the  $n$ th sample in the chain and  $\bar{E}$  is the mean energy of the Hamiltonian system for the whole chain. Ideally,

<sup>2</sup> This statistic has also been called the Bayesian Fraction of Missing Information (BFMI); however, the statistic is not specifically Bayesian and hence the shorter name is preferred.

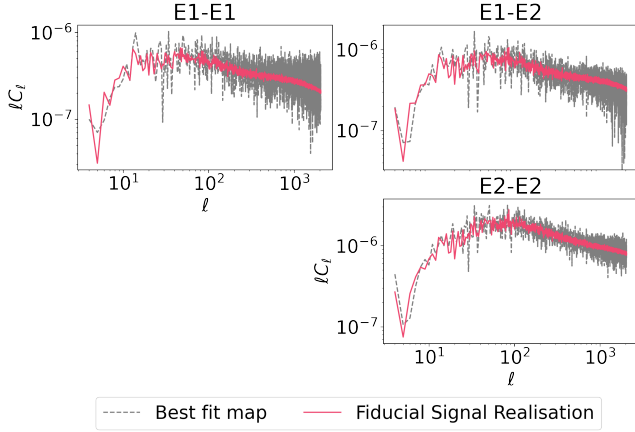


FIG. 11.—: Consistency check between the inferred shear maps and the simulated signal map showing the  $E$ -mode angular power spectra for a typical map. In red we show the angular power spectra for the signal realisation in the simulations, while in grey we show the pseudo- $C_\ell$  for the typical map.

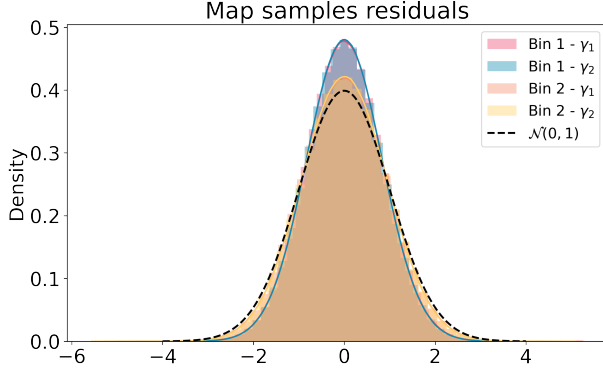
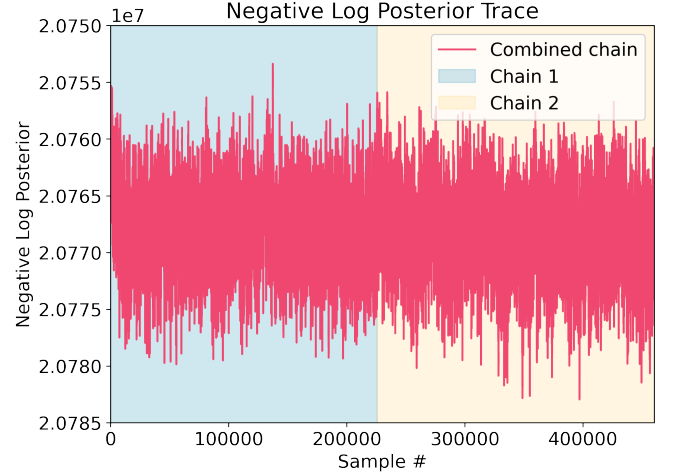


FIG. 12.—: Residuals from the samples of shear component maps obtained by ALMANAC compared to the underlying noiseless maskless signal map. The residuals are expected to be distributed as a standard normal (shown for comparison).

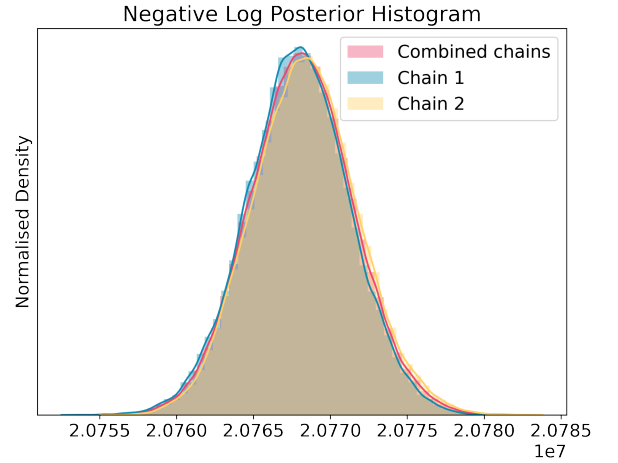
the FMI should be close to unity; we achieve a FMI of 0.87 for chain 1 and 0.84 for chain 2.

The requirement that FMI should be close to unity can be visualised by looking at the histograms of  $E = E_n - \bar{E}$  and  $\Delta E = E_n - E_{n-1}$  shown in Fig. 14 for both chains individually. Ideally, the two histograms should be close. Even with a very low S/N for the  $B$ -modes, Fig. 14 shows that the coordinate transformation discussed in Sec. 4 allows the HMC sampler to properly explore phase space (Betancourt 2016, 2017).

As a third test we compute the correlation length of individual chains; this is defined, for each parameter, to be the length at which the auto-correlation of the parameter values in the chain drops below a threshold of 0.1 for the first time. We find the chains have a median correlation length of 3042 and 2585, respectively, which corresponds to having a total of 165 fully independent samples in the chains. Both these tests demonstrate significant convergence for the individual chains, meaning that the two chains can be combined for more robust constraints.



(a) Log Posterior Trace



(b) Log Posterior Histogram

FIG. 13.—: Diagnostics for the log posterior for the two chains (both individually and combined). (a) The log posterior trace for the combined (i.e. concatenated) chain (blue region is chain 1, orange region is chain 2). (b) Combined (pink) and individual chain (blue and orange) histograms of the log posterior values.

As a fourth test we examine Hanson's convergence statistic (Hanson 2001; Taylor et al. 2008),

$$\mathcal{H}_i = \frac{\frac{1}{N} \sum_{n=1}^N (x_{n,i} - \bar{x}_i)^2}{\frac{1}{3N} \sum_n (x_{n,i} - \bar{x}_i)^3 \nabla_{x_i} \psi}, \quad (37)$$

where  $x_{n,i}$  is the  $n$ th sample of the  $i$ th parameter. Our  $\mathcal{H}$  equals that in Taylor et al. (2008) and is the reciprocal of that in Hanson (2001). For a distribution with exponentially decaying tails,  $\mathcal{H}_i$  is expected to tend to unity for all dimensions  $i$ , if convergence is reached.

Taylor et al. (2008) states that in practice,  $\mathcal{H}_i$  between 0.8 and 1.2 suggests good convergence in the chains. Fig. 15 shows this diagnostic applied to the spherical harmonic dimensions of the posterior; this demonstrates good convergence.

Finally, since we have two independent chains with different starting points, we can perform a Gelman-Rubin

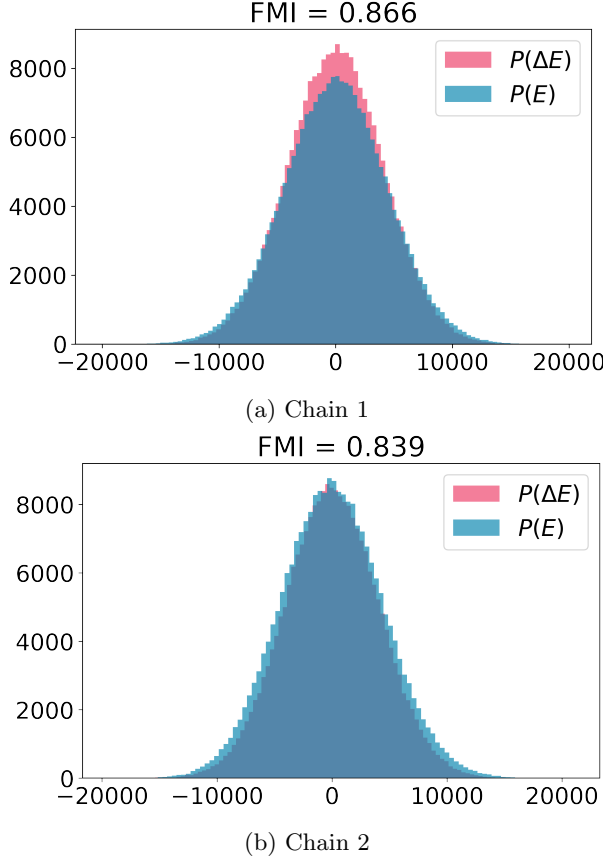


FIG. 14.—: Fraction of Missing Information histograms for the two chains.

test to further assess convergence. The results of this test are shown in Fig. 16 for each of the angular power spectrum dimensions. The median is very close to unity (1.0034) with a small tail to higher values. Although excellent convergence is not achieved for all dimensions, the overall distribution of marginalised angular power spectra demonstrates a satisfactory convergence. Hence, we are confident that the chains have converged to the correct posterior distribution.

## 7. DISCUSSION

This work presents a Bayesian hierarchical model for joint inference of angular power spectra and maps applied to simulated Stage IV tomographic cosmic shear data distributed on the sphere. The method hierarchically models the fields and their covariances, with a harmonic space parameterisation and a Cholesky decomposition of the power spectra.

This Bayesian approach has the advantage of producing samples of the posterior distribution of the power spectra and map coefficients, thereby avoiding the simplifying assumption of gaussianity that is a feature of summary statistics (and that may or may not be accurate). The posterior distribution has more than 16.8 million parameters, and is thus a challenge for a standard Bayesian approach to joint inference. Such a high-dimensional posterior requires an efficient sampler; we have developed a Hamiltonian Monte Carlo sampler with tuning stages to optimise the step-size and acceptance ratio (Sellentin, Loureiro et al., *in prep*). To deal with the

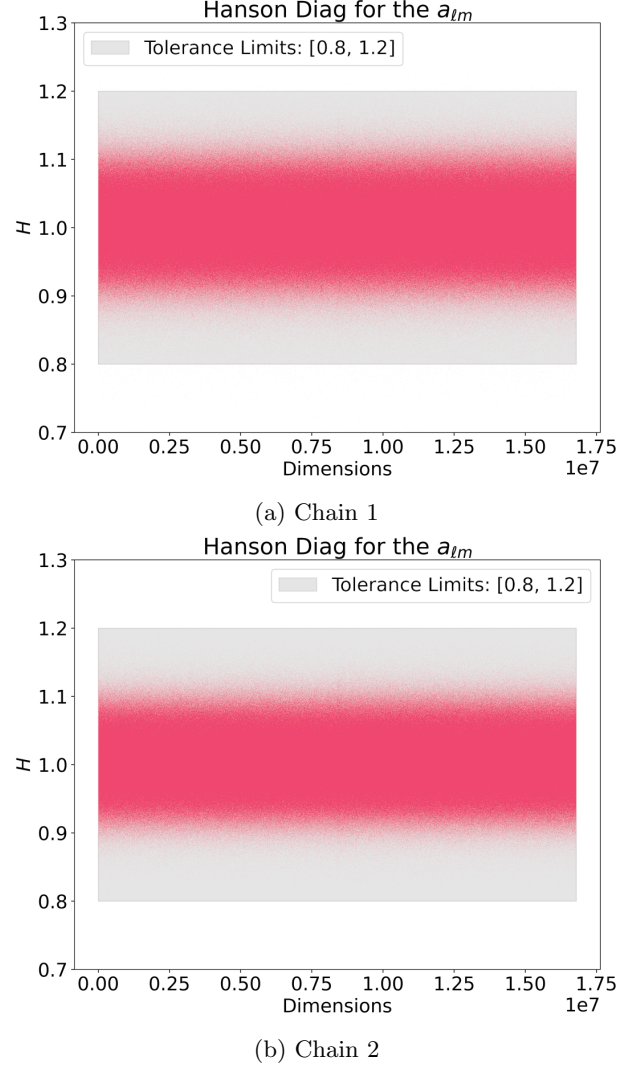


FIG. 15.—: Hanson diagnostics for the spherical harmonic coefficients. The quoted tolerance limits suggest good convergence (Taylor et al. 2008).

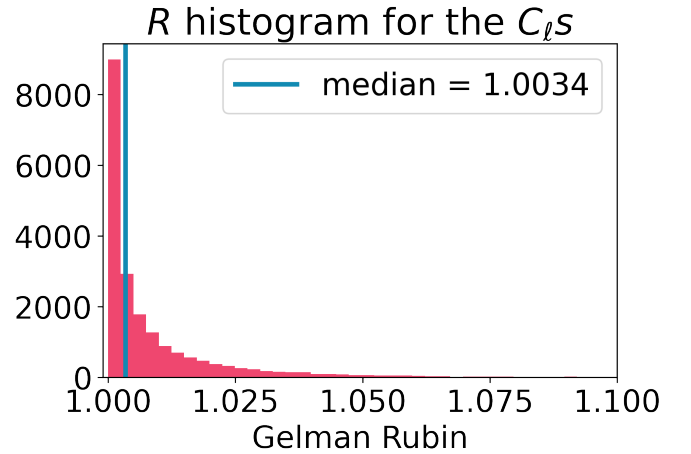


FIG. 16.—: Distribution of Gelman-Rubin  $R$  statistics, for the power spectra, for  $\ell_{\max} = 2048$ . A very small number of  $R$  values are larger than the range shown.

low S/N intrinsically found in the  $B$ -modes (expected to be zero for the standard cosmological model and usual extensions), we performed a coordinate transformation to both the spherical harmonic coefficients, by re-scaling them to their variance, and to the field’s covariance in harmonic space – described in Eq. (19) and (21).

Although past works have applied similar methods to cosmic shear data (Alsing et al. 2016, 2017), this is the first time this methodology has been developed for a complete lensing sky, without the flat-sky approximation. Moving away from the flat-sky approximation is crucial for analysing the next generation of cosmic shear surveys due to the significant increase in sky coverage compared to the previous generations (Lemos et al. 2017; Tutusaus et al. 2020; Matthewson & Durrer 2021). For the method presented here, we can use the increase in sky coverage to our advantage: as more modes are available in the observed data, ALMANAC can robustly infer the missing data under the mask and its angular power spectra.

To test the methodology, we simulated a Euclid-like survey using gaussian simulations to control the simulation’s signal, noise, and underlying angular power spectra. The simulations contained two tomographic bins with the expected Euclid mask, galaxy density, and shape noise. We then analysed the cosmic shear simulated data with two chains using different starting points over the multipole range  $4 \leq \ell \leq 2048$ . From this analysis, we inferred the angular power spectra of cosmic shear  $E$ - and  $B$ -modes from the simulated data. Here, we highlight the highly non-gaussian posterior distributions shown in Fig. 6 for the largest scales and how, even for scales larger than the ones available in data, we can still accurately infer the angular power spectra of the  $E$ -modes. Although the largest scales in the angular power spectra of cosmic shear carry little cosmological information, these scales allow us to reconstruct the inferred denoised shear maps, as shown in Sect. 6.2. We note, however, that such scales are extremely valuable for galaxy clustering studies with primordial non-gaussianities (Andrews et al. 2022; Baumann & Green 2022). We will study the effects of the non-gaussianities on the angular power spectra in a future work.

Since the method presented here also infers the spherical harmonic coefficients for the underlying signal, we can convert these samples into recovered signal maps for cosmic shear, convergence, and lensing potential. The maps we recover in each sample contain information inferred under areas where the telescope has not collected data. When naively analysing typical maps in the chains, we can recover a significant amount of information, but not sufficient to precisely recover the full signal for small scales (missing due to the mask). Nevertheless, in future works we will explore how the mass maps we recovered, under a gaussian signal assumption, compare to other mainstream mass mapping methods in the literature (Kaiser & Squires 1993; Marshall et al. 2002; Lanusse et al. 2016; Chang et al. 2018; Price et al. 2021; Jeffrey et al. 2021).

Differently from (pseudo) angular power spectrum estimators (Alonso et al. 2019; Nicola et al. 2021; Chon et al. 2004) or correlation function estimators (Jarvis et al. 2004; Kilbinger et al. 2014), here we are probing the full posterior distribution of full-sky  $E$ - and  $B$ -modes  $C_\ell$ . This allows us to inspect for systematic contamination in

parity-violating and  $B$ -modes. For point estimates, the mask can make it difficult to disambiguate between  $E$ -mode power and  $B$ -mode power. In some analyses this is described as ‘ $EB$  leakage’ for which various solutions are proposed (Schneider et al. 2010; Leistedt et al. 2017; Liu et al. 2019; Ghosh et al. 2021). With ALMANAC, on the other hand, we have the full posterior and such leakage does not occur. The ambiguity may simply show up as correlation between the  $E$  and  $B$  mode power spectra (and wider error bars on each power spectrum element individually), and we typically find the marginal distributions of  $B$ -mode power spectra to have a mode at zero, as we expect. Only if these posteriors are converted to point estimates would one expect such  $EB$  leakage to occur.

In comparison with other BHM’s for field-level inference, such as BORG (Jasche & Wandelt 2013; Jasche & Lavaux 2019; Porqueres et al. 2021, 2022), ALMANAC has the advantage of being agnostic to the underlying gravitational model, so the map and power spectra samples may be used to test many cosmological models. However, without a specific gravity model included, ALMANAC does not sample the initial conditions of the Universe.

In terms of computational resources for future Euclid and LSST applications, the method is limited by the spherical harmonic transformations performed using LIBSHARP2 (Reinecke & Seljebotn 2013; Ishioka 2018). For the set-up we presented in this work, we are able to produce 100 samples from the posterior distribution in less than 40 minutes on an Apple M1 Pro laptop<sup>3</sup>. Future investigations of parallelising the posterior calculations over redshift tomographic bins could potentially provide a significant speed-up in the calculations.

Future works will investigate extensions of ALMANAC to non-gaussian likelihoods and to the extraction of cosmological parameters via different approaches, including naively using the marginalised samples and their covariances for inference. We will also explore the use of the ALMANAC to galaxy clustering and to joint analysis of cosmic shear, galaxy clustering, and CMB.

#### ACKNOWLEDGMENTS

We thank the support staff of Leiden University’s ALICE High Performance Computing infrastructure and UCL’s Hypatia cluster, specially Edd Edmonson, Martin Reinecke for assistance with libsharp (Reinecke & Seljebotn 2013), and Malak Olamaie, Sree Balan, Mike Hobson, Joris Bierkens and Justin Alsing for useful discussions. ALMANAC was created by making significant modifications to a software package originally written by Sreekumar Balan and we record our gratitude to him for making this code available to us. The work we present here would not be possible without following packages and software: NUMPY (Harris et al. 2020), SCIPY (Virtanen et al. 2020), MATPLOTLIB (Hunter 2007), HEALPIX (Gorski et al. 1999), LIBSHARP 2 (Ishioka 2018), GETDIST (Lewy 2019), PANDAS (Wes McKinney 2010), ASTROPY (Astropy Collaboration et al. 2018) and JUPYTER LAB (Kluyver et al. 2016). This work used computing equipment funded by the Research Capital Investment Fund (RCIF) provided by UKRI, and

<sup>3</sup> Note, however, that the analysis was not performed on a laptop, but on local cluster computers.



is partially funded by the UCL Cosmoparticle Initiative.

## REFERENCES

- Alonso D., Sanchez J., Slosar A., LSST Dark Energy Science Collaboration 2019, *MNRAS*, **484**, 4127
- Alsing J., Heavens A., Jaffe A. H., Kiessling A., Wandelt B., Hoffmann T., 2016, *MNRAS*, **455**, 4452
- Alsing J., Heavens A., Jaffe A. H., 2017, *MNRAS*, **466**, 3272
- Amon A., Efstathiou G., 2022, *MNRAS*, **516**, 5355
- Amon A., et al., 2022, *Phys. Rev. D*, **105**, 023514
- Andrews A., Jasche J., Lavaux G., Schmidt F., 2022, arXiv e-prints, p. [arXiv:2203.08838](https://arxiv.org/abs/2203.08838)
- Asgari M., et al., 2019, *A&A*, **624**, A134
- Asgari M., et al., 2021, *A&A*, **645**, A104
- Astropy Collaboration et al., 2018, *AJ*, **156**, 123
- Bardeen J. M., Bond J. R., Kaiser N., Szalay A. S., 1986, *ApJ*, **304**, 15
- Bartelmann M., Maturi M., 2017, *Scholarpedia*, **12**, 32440
- Bartelmann M., Schneider P., 2001, *Phys. Rep.*, **340**, 291
- Baumann D., Green D., 2022, *J. Cosmology Astropart. Phys.*, **2022**, 061
- Betancourt M., 2016, arXiv e-prints, p. [arXiv:1604.00695](https://arxiv.org/abs/1604.00695)
- Betancourt M., 2017, arXiv e-prints, p. [arXiv:1701.02434](https://arxiv.org/abs/1701.02434)
- Betancourt M. J., Girolami M., 2013, arXiv e-prints, p. [arXiv:1312.0906](https://arxiv.org/abs/1312.0906)
- Blazek J., Vlah Z., Seljak U., 2015, *J. Cosmology Astropart. Phys.*, **2015**, 015
- Bunn E. F., 2008, arXiv e-prints, p. [arXiv:0811.0111](https://arxiv.org/abs/0811.0111)
- Bunn E. F., Zaldarriaga M., Tegmark M., de Oliveira-Costa A., 2003, *Phys. Rev. D*, **67**, 023501
- Casella G., George E. I., 1992, *The American Statistician*, **46**, 167
- Castro P. G., Heavens A. F., Kitching T. D., 2005, *Phys. Rev. D*, **72**, 023516
- Catelan P., Kamionkowski M., Blandford R. D., 2001, *MNRAS*, **320**, L7
- Chang C., et al., 2018, *MNRAS*, **475**, 3165
- Chisari N. E., et al., 2019, *ApJS*, **242**, 2
- Chon G., Challinor A., Prunet S., Hivon E., Szapudi I., 2004, *MNRAS*, **350**, 914
- Codis S., Jindal A., Chisari N. E., Vibert D., Dubois Y., Pichon C., Devriendt J., 2018, *MNRAS*, **481**, 4753
- Colombo L. P. L., et al., 2022, arXiv, p. 2208.14276
- DES Collaboration et al., 2022, *Phys. Rev. D*, **105**, 023520
- Eriksen H. K., et al., 2004, *ApJS*, **155**, 227
- Euclid Collaboration et al., 2020, *A&A*, **642**, A191
- Euclid Collaboration et al., 2022, *A&A*, **662**, A112
- Geman S., Geman D., 1984, *IEEE - Transactions on Pattern Analysis and Machine Intelligence*, pp 721–741
- Ghosh S., Delabrouille J., Zhao W., Santos L., 2021, *J. Cosmology Astropart. Phys.*, **2021**, 036
- Gorski K. M., Wandelt B. D., Hansen F. K., Hivon E., Banday A. J., 1999, arXiv e-prints, [pp astro-ph/9905275](https://arxiv.org/abs/pp_astro-ph/9905275)
- Gupta A.K. and Nagar D., 1999, *Matrix Variate Distributions*. Chapman & Hall/CRC, London
- Hajian A., 2007, *Phys. Rev. D*, **75**, 083525
- Hall A., 2021, *MNRAS*, **505**, 4935
- Hanson K. M., 2001, in Sonka M., Hanson K. M., eds, *Society of Photo-Optical Instrumentation Engineers (SPIE) Conference Series Vol. 4322, Medical Imaging 2001: Image Processing*. pp 456–467, [doi:10.1117/12.431119](https://doi.org/10.1117/12.431119)
- Harris C. R., et al., 2020, *Nature*, **585**, 357
- Hartlap J., Schrabback T., Simon P., Schneider P., 2009, *A&A*, **504**, 689
- Hastings W. K., 1970, *Biometrika*, **57**, 97
- Heavens A., 2009, *Nuclear Physics B Proceedings Supplements*, **194**, 76
- Heavens A., Refregier A., Heymans C., 2000, *MNRAS*, **319**, 649
- Heymans C., White M., Heavens A., Vale C., van Waerbeke L., 2006, *MNRAS*, **371**, 750
- Heymans C., et al., 2013, *MNRAS*, **432**, 2433
- Heymans C., et al., 2021, *A&A*, **646**, A140
- Hikage C., et al., 2019, *PASJ*, **71**, 43
- Hoffman Y., Ribak E., 1992, *ApJ*, **384**, 448
- Hunter J. D., 2007, *Computing in Science & Engineering*, **9**, 90
- Ishioka K., 2018, *Journal of the Meteorological Society of Japan. Ser. II*, **96**, 241
- Jarvis M., 2015, *TreeCorr: Two-point correlation functions*, Astrophysics Source Code Library, record ascl:1508.007 (ascl:1508.007)
- Jarvis M., Bernstein G., Jain B., 2004, *MNRAS*, **352**, 338
- Jasche J., Kitaura F. S., 2010, *MNRAS*, **407**, 29
- Jasche J., Lavaux G., 2019, *A&A*, **625**, A64
- Jasche J., Wandelt B. D., 2013, *MNRAS*, **432**, 894
- Jaynes E. T., 2003, *Probability theory: The logic of science*. Cambridge University Press, Cambridge
- Jeffrey N., et al., 2021, *MNRAS*, **505**, 4626
- Jewell J. B., Eriksen H. K., Wandelt B. D., O'Dwyer I. J., Huey G., Górski K. M., 2009, *ApJ*, **697**, 258
- Joachimi B., Bridle S. L., 2010, *A&A*, **523**, A1
- Joachimi B., et al., 2015, *Space Sci. Rev.*, **193**, 1
- Kaiser N., 1992, *ApJ*, **388**, 272
- Kaiser N., Squires G., 1993, *ApJ*, **404**, 441
- Kiessling A., et al., 2015, *Space Sci. Rev.*, **193**, 67
- Kilbinger M., 2015, *Reports on Progress in Physics*, **78**, 086901
- Kilbinger M., Bonnett C., Coupon J., 2014, *athena: Tree code for second-order correlation functions*, Astrophysics Source Code Library, record ascl:1402.026 (ascl:1402.026)
- Kirk D., et al., 2015, *Space Sci. Rev.*, **193**, 139
- Kluyver T., et al., 2016, in Loizides F., Schmidt B., eds, *Positioning and Power in Academic Publishing: Players, Agents and Agendas*. IOS Press, Netherlands, pp 87–90, <https://eprints.soton.ac.uk/403913/>
- LSST Science Collaboration et al., 2009, arXiv e-prints, p. [arXiv:0912.0201](https://arxiv.org/abs/0912.0201)
- Lanusse F., Starck J. L., Leonard A., Pires S., 2016, *A&A*, **591**, A2
- Larson D. L., Eriksen H. K., Wandelt B. D., Górski K. M., Huey G., Jewell J. B., O'Dwyer I. J., 2007, *ApJ*, **656**, 653
- Laureijs R., et al., 2011, arXiv e-prints, p. [arXiv:1110.3193](https://arxiv.org/abs/1110.3193)
- Leclercq F., Jasche J., Wandelt B., 2015, *J. Cosmology Astropart. Phys.*, **2015**, 015
- Leistedt B., McEwen J. D., Büttner M., Peiris H. V., 2017, *MNRAS*, **466**, 3728
- Lemos P., Challinor A., Efstathiou G., 2017, *J. Cosmology Astropart. Phys.*, **2017**, 014
- Lemos P., et al., 2021, *MNRAS*, **505**, 6179
- Lewis A., 2005, *Phys. Rev. D*, **71**, 083008
- Lewis A., 2019, arXiv e-prints, p. [arXiv:1910.13970](https://arxiv.org/abs/1910.13970)
- Liu H., Creswell J., von Hausegger S., Naselsky P., 2019, *Phys. Rev. D*, **100**, 023538
- Loureiro A., et al., 2022, *A&A*, **665**, A56
- MacCrann N., Zuntz J., Bridle S., Jain B., Becker M. R., 2015, *MNRAS*, **451**, 2877
- Mandelbaum R., et al., 2018, *PASJ*, **70**, S25
- Marshall P. J., Hobson M. P., Gull S. F., Bridle S. L., 2002, *MNRAS*, **335**, 1037
- Matthewson W. L., Durrer R., 2021, *J. Cosmology Astropart. Phys.*, **2021**, 027
- Metropolis N., Rosenbluth A. W., Rosenbluth M. N., Teller A. H., Teller E., 1953, *J. Chem. Phys.*, **21**, 1087
- Munshi D., Valageas P., van Waerbeke L., Heavens A., 2008, *Phys. Rep.*, **462**, 67
- Neal R. M., 2000, arXiv e-prints, p. [physics/0009028](https://arxiv.org/abs/physics/0009028)
- Neal R., 2011, in Brooks S., Gelman A., Jones G. L., Meng X.-L., eds, *Handbook of Markov Chain Monte Carlo*. Chapman & Hall/CRC, pp 113–162, [doi:10.1201/b10905](https://doi.org/10.1201/b10905)
- Nicola A., García-García C., Alonso D., Dunkley J., Ferreira P. G., Slosar A., Spergel D. N., 2021, *J. Cosmology Astropart. Phys.*, **2021**, 067
- Percival W. J., Friedrich O., Sellentin E., Heavens A., 2022, *MNRAS*, **510**, 3207
- Planck Collaboration et al., 2020, *A&A*, **641**, A6
- Porqueres N., Heavens A., Mortlock D., Lavaux G., 2021, *MNRAS*, **502**, 3035
- Porqueres N., Heavens A., Mortlock D., Lavaux G., 2022, *MNRAS*, **509**, 3194
- Price M. A., McEwen J. D., Pratley L., Kitching T. D., 2021, *MNRAS*, **500**, 5436

- Racine B., Jewell J. B., Eriksen H. K., Wehus I. K., 2016, *ApJ*, **820**, 31
- Reinecke M., Seljebotn D. S., 2013, *A&A*, **554**, A112
- Rossi G., 2012, *MNRAS*, **421**, 296
- Schneider P., 2005, arXiv e-prints, [pp astro-ph/0509252](https://arxiv.org/abs/pp astro-ph/0509252)
- Schneider P., Eifer T., Krause E., 2010, *A&A*, **520**, A116
- Secco L. F., et al., 2022, *Phys. Rev. D*, **105**, 023515
- Sellentin E., Heavens A. F., 2016, *MNRAS*, **456**, L132
- Sellentin E., Heavens A. F., 2018, *MNRAS*, **473**, 2355
- Sellentin E., Heymans C., Harnois-Déraps J., 2018, *MNRAS*, **477**, 4879
- Taylor J. F., Ashdown M. A. J., Hobson M. P., 2008, *MNRAS*, **389**, 1284
- Taylor P. L., et al., 2021, *The Open Journal of Astrophysics*, **4**, 6
- Tutusaus I., et al., 2020, *A&A*, **643**, A70
- Upham R. E., et al., 2022, *A&A*, **660**, A114
- Van Waerbeke L., et al., 2013, *MNRAS*, **433**, 3373
- Virtanen P., et al., 2020, *Nature Methods*, **17**, 261
- Wallis C. G. R., Price M. A., McEwen J. D., Kitching T. D., Leistedt B., Plouviez A., 2022, *MNRAS*, **509**, 4480
- Wandelt B. D., Larson D. L., Lakshminarayanan A., 2004, *Phys. Rev. D*, **70**, 083511
- Wes McKinney 2010, in Stéfan van der Walt Jarrod Millman eds, *Proceedings of the 9th Python in Science Conference*. pp 56 – 61, [doi:10.25080/Majora-92bf1922-00a](https://doi.org/10.25080/Majora-92bf1922-00a)

This paper was built using the Open Journal of Astrophysics L<sup>A</sup>T<sub>E</sub>X template. The OJA is a journal which

provides fast and easy peer review for new papers in the **astro-ph** section of the arXiv, making the reviewing process simpler for authors and referees alike. Learn more at <http://astro.theoj.org>.